



HAL
open science

Temperature Rise Caused by Shear Wave Elastography, Pulse Doppler and B-Mode in Biological Tissue: An Infrared Thermographic Approach

Maha Issaoui, Xavier Balandraud, Michel Grédiac, Benoît Blaysat, Lemlih × Ouchchane, Amelie Delabaere, Marie-Pierre Sauvante-Rochat, Didier Lemery

► **To cite this version:**

Maha Issaoui, Xavier Balandraud, Michel Grédiac, Benoît Blaysat, Lemlih × Ouchchane, et al.. Temperature Rise Caused by Shear Wave Elastography, Pulse Doppler and B-Mode in Biological Tissue: An Infrared Thermographic Approach. *Ultrasound in Medicine & Biology*, 2020, 46 (2), pp.325-335. 10.1016/j.ultrasmedbio.2019.10.008 . hal-03026025

HAL Id: hal-03026025

<https://hal.science/hal-03026025v1>

Submitted on 21 Jul 2022

HAL is a multi-disciplinary open access archive for the deposit and dissemination of scientific research documents, whether they are published or not. The documents may come from teaching and research institutions in France or abroad, or from public or private research centers.

L'archive ouverte pluridisciplinaire **HAL**, est destinée au dépôt et à la diffusion de documents scientifiques de niveau recherche, publiés ou non, émanant des établissements d'enseignement et de recherche français ou étrangers, des laboratoires publics ou privés.



Distributed under a Creative Commons Attribution - NonCommercial 4.0 International License

1 **Temperature rise caused by Shear Wave Elastography,**
2 **Pulse-Doppler and B-mode in biological tissue: an infrared**
3 **thermographic approach**

4
5 Maha Issaoui^a, Xavier Balandraud^a, Michel Grédiac^a, Benoit Blaysat^a, Lemlih Ouchchane^{b,c},
6 Amelie Delabaere^{b,d}, Marie-Pierre Sauvant-Rochat^{a,e}, and Didier Lemery^{b,d}

7
8 ^a Université Clermont Auvergne, CNRS, SIGMA Clermont, Institut Pascal, F-63000
9 Clermont-Ferrand, France

10 ^b Université Clermont Auvergne, CHU Clermont-Ferrand, CNRS, SIGMA Clermont, Institut
11 Pascal, F-63000 Clermont-Ferrand, France

12 ^c Département de Santé Publique, Unité de Biostatistique et Informatique Médicale, CHU de
13 Clermont-Ferrand, F-63000 Clermont-Ferrand, France

14 ^d Pôle Femme et Enfant, Centre Hospitalier Universitaire de Clermont-Ferrand, F-63000
15 Clermont-Ferrand, France

16 ^e Département de Santé Publique et Environnement, Université Clermont-Auvergne, UFR
17 Pharmacie, F-63000 Clermont-Ferrand, France.

18
19 Address correspondence to: Maha Issaoui, Université Clermont Auvergne, CNRS, SIGMA
20 Clermont, Institut Pascal, F-63000 Clermont-Ferrand, France. E-mail:

21 maha.issaoui@etu.uca.fr

22

23 **Abstract**—The aim of the study is to demonstrate the interest and relevance of infrared
24 thermography, which is a non-invasive full-field surface temperature measurement technique,
25 to characterize the heterogeneous heating caused by ultrasound in biological tissue. Thermal
26 effects of Shear Wave Elastography (SWE), Pulse-Doppler (PD) and B-mode were evidenced
27 in porcine tissue. Experiments were performed using a high-frequency echography
28 Aixplorer® system (Supersonic Imagine, Aix-en-Provence, France). For the three modes,
29 ultrasound was applied continuously for 360 seconds while the temperature was recorded at
30 the sample surface with a Cedip Jade III-MWIR infrared camera (Flir, Torcy, France).
31 Temperature changes were detected for the three modes. In particular, “heat tunnels” crossing
32 the sample were visualized from the early stages of the experiment. Heat conduction from the
33 transducer was also involved in the global warming of the sample. The study opens up
34 prospects for safety studies, potentially in addition to classical approaches such as those using
35 thermocouples.

36

37 **Keyword:** Shear Wave Elastography; Ultrasound; Infrared thermography; Temperature rise;
38 Safety

39

40

41

INTRODUCTION

42

43 Shear Wave Elastography (SWE) exploits acoustic radiation force (ARF) to generate stiffness
44 maps in biological tissue. In practice, a 100 μs focused compression wave generates radiation
45 force in dissipative biological media, which pushes the tissue for some dozens of μm in the
46 target focal zone. When the tissue relaxes, it creates a shear wave propagating perpendicularly
47 to the axis of the ultrasound beam at a speed of about 1 m/s. This shear wave is then
48 visualized by ultrafast ultrasound imaging, capturing the wave front every 10 ms. Shear wave
49 propagation speed is related to the Young's modulus of the biological tissue, a physical
50 property usually expressed in kPa and characterizing material stiffness (Genisson et al.
51 2013). The clinical relevance of SWE has been demonstrated for the detection of masses in
52 superficial organs such as breast cancer (Cosgrove et al. 2012), and for the diagnosis of
53 pathologies in deep organs, such as a cirrhotic liver (Guibal et al. 2016).

54 With the increasing number of publications on elastography, the World Federation for
55 Ultrasound in Medicine and Biology (WFUMB) decided to take the initiative to create
56 guidelines in August 2011. The first consensus meeting was held in March 2013 and led to the
57 development of guidelines for basic science in elastography (Shiina et al. 2015), and for the
58 use of this technique for the breast (Barr et al. 2015) and liver (Ferraioli et al. 2015), without
59 distinguishing between the different elastography modes.

60 Elastography has recently been applied to gynecology (Thomas et al. 2007; Ami et al.
61 2009) and obstetrics (Kiliç et al. 2015; Alan et al. 2016; Quarello et al. 2016). Many
62 published articles already deal with tissues that are accessible to methods necessitating the
63 direct compression of the organ by the ultrasound probe, such as the cervix (Molina et al.
64 2012; Khalil et al. 2013; Hernandez-Andrade et al. 2014; Fruscalzo et al. 2016; O'Hara et al.

65 2018). Since SWE enables imaging without direct contact between the transducer and the
66 observed tissue, it appears as the ideal candidate for fetal tissue elastography examinations
67 (Diguisto et al. 2017; Mottet et al. 2017). However, until now there have been no guidelines
68 on the use of SWE in obstetrics. Regardless of its clinical relevance, it is necessary to
69 demonstrate its safety before allowing its utilization in routine practice for fetuses.

70 **Diagnostic** ultrasound can lead to two main types of potential effects on biological
71 tissues, namely thermal and mechanical effects (Shankar and Pagel 2011a). The thermal effect
72 was for instance studied by Palmeri and Nightingale (2004) using thermocouples placed
73 inside the tissue (Palmeri et Nightingale 2004). It is important to note that the period of
74 organogenesis is considered as particularly sensitive to thermal stress (Fowlkes 2008).
75 Investigations on laboratory animals have documented that an elevation in temperature can
76 damage biological tissues (Pellicer et al. 2011; Schneider-Kolsky et al. 2009). Thermally-
77 induced teratogenesis has been shown in many animal studies (Germain et al.1985). The issue
78 of temperature rise due to ultrasound, and SWE in particular, is thus critical.

79 In the present work, we focus on the observation of the thermal effect in biological
80 tissue generated by three ultrasonic modes, namely SWE, Pulse-Doppler (PD) and B-mode.
81 An infrared (IR) thermographic camera was used for this purpose. This device provides full-
82 field temperature measurements at the surface of the object under investigation. In the last few
83 decades, IR thermography has become widespread in the mechanics of materials community,
84 leading to important insights into the thermal response of materials subjected to mechanical
85 **excitation** (Chrysochoos et al. 2010). It is in particular possible to experimentally evidence
86 thermo-mechanical couplings, i.e. temperature variations caused by changes in the mechanical
87 state of the material. Various mechanical phenomena in various materials are related to
88 calorific responses, for instance elasticity, plasticity, viscosity, fatigue damage, elasto-plastic
89 transition, cracking, vibrations, friction, strain- or stress-induced phase transitions, etc. IR

90 thermography is now recognized as a relevant experimental means to study the
91 thermomechanics of materials. However, to the best of the authors' knowledge,
92 thermographic approaches have not before been applied to the calorific response of biological
93 tissues subjected to ultrasonic excitation.

94 The aim of the present study is to demonstrate the interest and the relevance of IR
95 thermography to characterize the heterogeneous heating caused by ultrasound in biological
96 tissue. Two modalities which are already authorized for pregnant women (PD and B-mode)
97 were compared with the SWE mode, with potential perspectives for the study of the safety of
98 the latter in obstetrics (Issaoui et al. 2018).

99

100 **MATERIALS AND METHODS**

101

102 *Experimental setup*

103

104 The echography system used for the experiments was a high-frequency Aixplorer®
105 (Supersonic Imagine, Aix-en-Provence, France). It features three **imaging** modes: B-Mode,
106 PD and SWE. The chosen transducer, typically used in obstetrics, was a curved SC6-1 probe
107 (Supersonic Imagine, Aix-en-Provence, France) featuring 192 piezoelectric elements and a
108 bandwidth of 1-6 MHz. Temperature measurements were carried out using a Cedip Jade III-
109 MWIR camera (Flir, Torcy, France). This IR camera features a wavelength range of 3.5-5 μm ,
110 a sensor size of 320×240 pixels and a Noise Equivalent Temperature Difference (NETD)
111 equal to 0.02°C. This latter quantity corresponds to the temperature measurement resolution,
112 that is, the change in quantity being measured that causes a change in the corresponding
113 indication of greater than one standard deviation of the measurement noise (Chrysochoos and

114 Surrel 2012). The lower the measurement resolution, the lower the noise and thus the better
115 the measurement.

116 Measurements were performed on homogeneous pieces of porcine muscle
117 (slaughterhouse: Hassenforder et fils S.A.S., Vichy, France; identification number: 11P18025;
118 FR-03-094-001 CE; order number; CV18032542) by three operators (MI, XB and DL).
119 Several samples with dimensions of $130 \times 70 \times 60 \text{ mm}^3$ were cut by hand. Two configurations
120 were tested in terms of the location of the transducer with respect to the porcine sample (Fig.
121 1-a). The reason for this positioning on the sample was that IR thermography provides
122 temperature maps at the surface of the observed object. In Configuration #1, the surface
123 observed by the IR camera is perpendicular to the plane of the transducer, whereas it is
124 parallel to it in Configuration #2. The two test configurations were considered as
125 complementary in order to obtain two perpendicular slices of the three-dimensional
126 temperature field in the bulk. It is worth noting that air is a bad conductor of heat by natural
127 convection, while pig muscle transmits heat relatively well by conduction (thermal diffusivity
128 of $1.14 \times 10^{-7} \text{ m}^2/\text{s}$ (Giering et al. 1995). Temperature rises during experiments are expected to
129 be overestimated compared to a situation for which the dimensions of the sample were
130 infinite.

131 A second sample was used as a reference to track thermal fluctuations in the close
132 environment (Fig. 1-b). The sample to be subjected to ultrasound (named “sample” in the
133 following) and the reference sample (named “reference” in the following) were placed in a
134 homemade plastic frame featuring two shelves. The reference was placed under the sample, in
135 the IR camera’s field of view. The bottom part of the transducer was also visible at the top of
136 the thermal images. Note that the reference was placed close enough to the sample so that it
137 can be reasonably assumed that it was submitted to the same environmental fluctuations

138 during testing. However, the reference was physically separate from the sample, so it was not
139 affected by ultrasonic excitation.

140 Figure 1-c shows three photographs of the experiment. The transducer was in contact
141 with the sample using a static system ensuring a constant force. The sample was therefore
142 deformed in addition to the effect of gravity. It is worth noting that performing quantitative
143 measurements with an IR camera is somewhat tricky when temperature changes are small.
144 This is due to the fact that various phenomena potentially influence the measured
145 temperatures in addition to the desired ones, for instance potential changes in the ambient
146 airflow or in ambient temperature, and more generally in the elements inside the testing room
147 (persons, heating system, doors opened, etc.). Misleading conclusion could therefore be
148 drawn from measured temperature fields if some precautions are not taken when preparing
149 and performing the tests. First, a cardboard tunnel was placed between the IR camera and the
150 observed surfaces. Second, attention was paid to ensure the steady thermal state of the testing
151 room. To this end, the echography system, IR camera and computers were turned on three
152 hours before the test session began, and nobody was present in the room during the tests, in
153 order to limit airflow. No operator was required to maintain the transducer/sample contact
154 thanks to the use of a fixed gripping system. Operators left the room just after starting the test,
155 whose end was programmed automatically. Thermal acquisition began twenty seconds before
156 starting ultrasonic excitation. Synchronization uncertainty was of about 0.5 s because of the
157 thermal recording frequency f_R set to 2 Hz, which is acceptable when considering the
158 response time of the thermal phenomena and the test duration.

159 The three echography modes (B-mode, PD and SWE) were applied for comparison
160 purposes, using a gel for the coupling between sample and transducer. Table 1 provides the
161 ultrasound parameters for each mode. For the three modes, the ultrasonic excitation ran
162 continuously for 360 s and then stopped. For each test, the IR camera measurements lasted

163 longer than this, so that temperature variations could be monitored after the ultrasonic activity
164 had stopped. A waiting time of one hour was respected between two consecutive tests, to
165 ensure a thermal steady state when starting the second one. Note that for the B-mode, two
166 focal configurations were also compared (10-25 mm and 25-40 mm), but preliminary tests
167 showed that there was no difference in terms of temperature distributions, probably due to low
168 calorific impact in both cases. Finally, the spatial resolution of the measured temperature
169 maps was 0.53 mm. In the metrological framework of full-field measurement techniques, the
170 spatial resolution can be defined as the period of the sine quantity beyond which the relative
171 loss in amplitude of the quantity returned by the measuring technique is greater than a certain
172 value (Grédiac et al. 2017). Basically, the spatial resolution can be seen as the shortest
173 distance between two spatially independent measurements. For raw thermal data provided by
174 an IR camera featuring independent sensors, the spatial resolution is equal to the pixel size
175 projected on the surface under investigation. Each temperature map can thus be seen as a grid of
176 “thermocouples” with a pitch equal to 0.53 mm.

177

178 *Measurement of temperature change due to ultrasonic excitation*

179

180 The calibration of the temperature measurement was performed by XB using a SR-
181 800-7D extended area blackbody (CI-systems) with a two-point procedure (10°C and 35°C)
182 and an integration time of 1500 μ s. The thermal emissivity of the biological tissue was
183 considered to be equal to 0.95, with an environment temperature corresponding to the ambient
184 temperature (between 24°C and 26°C **over the whole duration of the test period**). The thermal
185 emissivity value was defined after preliminary tests comparing temperature changes with and
186 without covering the raw surface of the biological tissue with matt black paint. Results
187 evidenced the high thermal emissivity of the raw surface of the sample. Two precautions were

188 taken to ensure the correct assessment of the temperature changes due to ultrasound: (i) the
189 use of specific thermal acquisition conditions to reduce noise, and (ii) the subtraction of
190 thermal fluctuations in the environment thanks to the reference.

191 (i) The IR camera acquisition frequency f_A was set to 100 Hz, but each recorded
192 image was the average of 50 successive frames, thus leading to a recording frequency f_R of
193 2 Hz. This setting was chosen based on preliminary tests (not detailed here) which showed
194 that the temperature change is smooth enough whatever echography mode is chosen. Indeed,
195 no “sudden” temperature increase could be observed. Averaging enables us to improve
196 measurement resolution compared to the base NETD of the IR camera, but without losing
197 information (see for instance (Gonzales and Woods 2006)). In theory, for Gaussian noise, the
198 temporal averaging operation of 50 frames improves the measurement resolution by a factor
199 of $\sqrt{50}$ but this impairs the temporal resolution. Applying this procedure leads the standard
200 deviation of the resulting noise to be equal to some thousandths of one degree only.

201 (ii) Figure 2 illustrates the interest of using the reference for the correct assessment of
202 the temperature change due to ultrasound only. The data correspond here to a test performed
203 in Configuration #1 for the B-mode. The black curve shows the temperature change of the
204 reference, while the blue one shows the temperature at point A on the sample subjected to
205 ultrasound (see schematic view in Figure 2 for the location of point A). By “point”, we mean
206 the surface element on the sample plane corresponding to one pixel, whose dimension is
207 $0.53 \times 0.53 \text{ mm}^2$. Note that the measurement resolution of the reference temperature was
208 improved by spatially averaging over a large rectangular zone (see schematic view in Figure
209 2). The red curve corresponds to the temperature change at point A due to ultrasonic waves
210 only, obtained by subtracting the temperature change of the reference from that of the sample.
211 Even if fluctuations in the environment (black curve) were limited to a few hundredths of a
212 degree, it can be seen that the raw data at point A slightly underestimates the data to be

213 considered for the analysis (the blue curve is below the red one). It is worth noting that the
214 “strong” perturbation around time 120 s was correctly removed by the processing.

215

216

RESULTS

217

218 For the sake of clarity, physical measurements are commented in the present section while the
219 clinical impact is developed in the following one.

220

221 *Analysis of some temperature change maps*

222

223 Figure 3 presents the maps of temperature change at $t = 80$ s in Configuration #1 for
224 the three echography modes. This specific time was selected to highlight the *remote* heating
225 from the transducer. The following comments can be drawn from this figure:

226 • for the three modes, a vertical “heat tunnel” is visible under the contact with the

227 transducer (see the arrows in the images). This phenomenon cannot be explained by an

228 increase in the transducer temperature accompanied by heat conduction inside the

229 sample. Indeed, assuming isotropic thermal conduction in the tissue, a concentric

230 distribution would have been obtained if only heat conduction was involved. Note,

231 however, that a conduction effect can be observed just under the contact with the

232 transducer, especially for the SWE mode (see green color in Fig. 3-c). This is a

233 consequence of the self-heating of the piezoelectric elements themselves;

234 • the vertical tunnels appear to be quite homogeneous in temperature for both the B-

235 mode (Fig. 3-a) and PD (Fig. 3-b): see homogeneous green color corresponding to a

236 temperature change lying between about 0.04°C and 0.06°C . For SWE, hotter zones

237 are clearly visible at the bottom part and some centimeters under the contact with the

238 transducer (Fig. 3-c). This latter observation confirms the *remote* heating from the
239 transducer, which is due to the ultrasonic waves crossing the sample in the plane of the
240 transducer. The hot zone at the bottom part can be explained by a reflection of the
241 waves, whereas the hot zone under the contact with the transducer can be explained by
242 an effect of beam focusing. This second hot zone appears to be located about 20 mm
243 under the contact with the transducer in the observation plane, to be compared with the
244 focal zone of 25-40 mm given in Table 1. The difference can be explained by recalling
245 that the transducer is curved. The hot zone is probably also curved inside the sample,
246 explaining the measurement of 20 mm in the observation plane;

- 247 • in order to have better color dynamics for each mode individually, Figure 3-d shows
248 some close-up views of the central zone with suitable color scales. With these
249 representations, reflections at the bottom part of the sample are also visible for the B-
250 mode. Clearly, the caloric effect of SWE in the biological tissue is greater than that of
251 both B-mode and PD.

252 As a general conclusion from Figure 3, the three heat tunnels in the temperature change maps
253 constitute a clear signature of remote heating from the transducer, associated with wave
254 propagation.

255 Figure 4 presents the thermal maps obtained for Configuration #1 at the end of
256 transducer activation, i.e. at $t = 360$ s. For B-mode and PD (Figs. 4-a and -b), the color scales
257 are the same as in Figure 3, for comparison purposes. For SWE, the color scale was modified
258 because of the much stronger thermal activity for this mode. As a first comment, the heat
259 tunnels can again be observed, but they appear thicker compared to those obtained at $t = 80$ s
260 (Fig. 3). Moreover, their widths are not homogeneous: they are indeed larger at their ends
261 (close to the transducer and at the bottom). This can be explained by heat conduction inside
262 the tissue: the heat that was created *remotely* by the waves progressively diffused. As a

263 general comment, temperature distribution is the result of three causes: the heat source
264 produced by wave propagation, heat conduction inside the tissue, and the heat exchanged with
265 the sample environment (by convection with ambient air and by contact with both the frame
266 and the transducer).

267 Figure 5 presents the temperature change maps for $t=360$ s for Configuration #2 and
268 for the three echography modes. The magnitude of temperature increase is globally greater
269 than for Configuration #1 at the same time (see Figure 4). The link between the data for the
270 two configurations will be discussed in the next section. In the measurement plane observed
271 with Configuration #2, the highest temperature changes in the sample are located close to the
272 transducer, which can be explained by heat transfer through contact. Heat tunnels similar to
273 those observed for Configuration #1 are visible, although they are more difficult to visualize
274 (dark blue).

275 It is worth noting that such features can only be observed and quantified thanks to a
276 full-field thermal measurement technique.

277

278 *Analysis of the temperature time variation*

279

280 Figure 6 shows the temperature change as a function of time at two points A and B, for
281 Configurations #1 and #2 respectively, for the three echography modes. The locations of these
282 points were chosen because they correspond to the most intense heating zones. The vertical
283 dashed lines correspond to the end of transducer activation, i.e. at time $t = 360$ s. Several
284 comments can be made with respect to this figure:

- 285 • SWE generates greater temperature changes for both configurations. PD causes a
286 larger increase in temperature than B-mode. This result is in agreement with previous
287 studies, see Ref. (Miloro et al. 2017) for instance. The difference in noise level

288 between Configurations #1 or #2 might be explained by the small movements of the
289 physical points observed by the IR camera at the specimen surface. Such movements
290 can potentially be due to oscillations caused by mechanical waves. The noise level
291 would thus depend on the orientation of the surface observed (Configurations #1 or
292 #2) with respect to the wave plane;

- 293 • for Configuration #2, the temperature clearly still increases for several tens of seconds
294 after halting the ultrasonic excitation (Fig. 6-b). This phenomenon can be explained by
295 the fact that heat is still transferred from the “hot” transducer. This confirms that, in
296 addition to *remote* heating, heat conduction is also involved;
- 297 • as indicated in the “Materials and methods” section, Configurations #1 and #2 were
298 initially considered as complementary, to obtain two perpendicular slices of the tri-
299 dimensional temperature field in the bulk. This approach appears to be reasonable
300 when comparing Figures 6-a and 7. The latter presents the temperature change as a
301 function of time for another point (named C) in Configuration #2. This point is at the
302 same location with respect to the transducer as point A in Configuration #1: see the
303 schematic view at the top of Figure 7. At time $t = 360$ s for the B-mode, the
304 temperature increase is nearly equal to 0.3°C for both Configurations #1 and #2
305 (compare the green curves in Figures 6-a and 7), thus validating the approach.
306 Similarly, the temperature increase for PD at $t = 360$ s is nearly equal to 0.4°C for both
307 configurations (compare the blue curves in Figures 6-a and 7);
- 308 • a specific remark can be made concerning the SWE mode. At $t = 360$ s, the
309 temperature change is nearly equal to 1.17°C for both configurations (compare the red
310 curves in Figures 6-a and 7), but the temperature continues to increase in
311 Configuration #2 after $t = 360$ s, reaching 1.56°C . This difference between the two
312 curves can be explained by the fact that points A and C are not exactly equivalent. For

313 instance, it can be noted that the hatched zone in Configuration #2 is not present in
314 Configuration #1 (Fig. 7). This effect of thermal inertia is also visible in Figure 7 for
315 both PD and B-mode, even if it is less pronounced than for SWE. The delay before
316 starting the return to ambient temperature can be explained by a competition between
317 heat loss by convection with the ambient air and heat absorption by contact with the
318 transducer. The latter is hotter than the tissue, and thus transfers heat to it.

319

320 Finally, Figures 8, 9 and 10 provide the temperature change as a function of time for the B-
321 mode, PD and SWE respectively, at various points and for both configurations. The location
322 of these points is reported in Figure 8-a for Configuration #1 and in Figure 8-b for
323 Configuration #2. Point P1 corresponds to point A in Figure 6-a (Configuration #1), while
324 Point P8 corresponds to point B in Figure 6-b (Configuration #2). An additional point (P0)
325 was directly placed on the transducer in Configuration #2, enabling us to capture the highest
326 temperature change in the thermal scene. It can be observed that, at the end of the ultrasonic
327 excitation (at $t = 360$ s), the temperature of the transducer reaches 0.95°C for the B-mode and
328 PD, and 1.95°C for SWE. Close to the transducer, heat conduction by contact is not
329 negligible. Note that the noise in the curves in Figures 8-a (B-mode in Configuration #1) and
330 9-a (PD in Configuration #1) appears to be greater than in the other curves, merely because of
331 the scale used for the y-axis. As already noted above, B-mode and PD are less calorific than
332 SWE.

333

334

DISCUSSION

335

336 Elastography, including SWE, is commonly used in various clinical applications (Cosgrove et
337 al. 2012; Guibal et al. 2016). Potential indications of SWE in fetal and uterine imaging during

338 pregnancy are cervix examination (Fruscalzo et al. 2016), and more importantly the
339 monitoring of fetal development. Recently, SWE was used to explore the fetal brain (Diguisto
340 et al. 2017) and lung (Mottet et al. 2017). In these studies, the authors considered that the
341 benefit-to-risk ratio of this technique was favorable. However, a recent review was unable to
342 demonstrate the safety of SWE regarding the fetus (Issaoui et al. 2018). Palmeri and
343 Nightingale (2004), Nitta et al. (2001) and Bouchard et al. (2009) studied the temperature rise
344 created by ARF in soft tissue (porcine muscle) by using thermocouples (Palmeri et
345 Nightingale 2004; Bouchard et al. 2009; Nitta et al. 2015). Skurczynski et al. (2009) analyzed
346 the temperature increase and the cavitation effect by performing focused **diagnostic**
347 ultrasound: they reported a potential heating risk during elasticity measurement by ARF when
348 a bone is present (Skurczynski et al. 2009). The effect of temperature rise potentially leading
349 to the teratogenesis of developing tissues was evidenced *in vivo* in animal models. This effect
350 is documented in Refs (Hinoue et al. 2001; Church and Miller 2007; Abramowicz et al. 2008;
351 Shankar and Pagel 2011b). Abnormalities include growth retardation, microencephaly,
352 cataract, and other malformations (Ziskin and Morrissey 2011). Some *in vivo* experiments
353 have also shown that the threshold temperature increase for teratogenic effects induced by
354 hyperthermia is estimated at 1.5°C for an exposure of 5 min (Abramowicz 2002; Abramowicz
355 et al. 2008). A major problem with formulating hypotheses from animal data is that *in vivo*
356 effects of hyperthermia seen in animals result from exposure situations that would never be
357 encountered by the human embryo or fetus during ultrasound examination. However, a review
358 of the literature by Marinac-Dabic et al. (2002) identified the epidemiologic studies focusing
359 on human exposure to diagnostic ultrasound during pregnancy and the potential associations
360 between *in utero* ultrasound exposure and growth restriction, delayed speech, dyslexia and
361 non-right-handedness. The authors concluded that there was no association between *in utero*
362 exposure to ultrasound and either growth restriction or delayed speech. There are,

363 nonetheless, some questions about non-right-handedness after frequent exposure to Doppler
364 ultrasound. However, no definitive conclusions can yet be drawn. To date no study has
365 specifically looked at the effects of SWE.

366 In this context, developing experimental techniques to measure the temperature rise in
367 biological tissue caused by ultrasound is of prime interest. Thermocouples placed inside the
368 tissue are classically employed and have proved to be efficient. The present study shows that
369 IR thermography could be a complementary experimental approach. This technique provides
370 temperature maps without contact with the tissue, thus avoiding the potential artefacts that
371 thermocouples may cause. Indeed, since ARF creates a matter displacement, it is difficult to
372 know to what extent a thermocouple will generate a secondary ultrasound source (thus
373 creating a secondary heat source).

374 A limitation of our study is that it was performed on samples containing only soft
375 tissues: our samples did not contain bone parts. Many other studies have shown that the
376 thermo-sensitivity of bone is much higher than that of soft tissues (Skurczynski et al. 2009;
377 Nitta et al. 2015; Tabaru et al. 2012). In fact, a fetus is composed principally of soft tissues
378 but also of bones. For obvious ethical reasons however, it was impossible to perform these
379 tests on fetal tissues. Further studies should be performed on phantoms containing soft tissues
380 and bones.

381 The strength of the present test **procedure** is that precautions were taken to avoid
382 potential misinterpretation of the results: a waiting time before starting any new test from an
383 initial thermal steady state, the subtraction of parasitic effects thanks to a reference sample,
384 and noise reduction. It can be noted that, as usual for full-field measurement techniques, huge
385 amounts of data were recorded (videos of several hundreds of **megabytes** for each test) and
386 processed. After preliminary tests, the experiments were repeated twice in order to check that
387 the results were similar. Let us recall that the objective of the study was not to perform a

388 statistical analysis of the results, but to demonstrate the relevance of IR thermography as an
389 experimental tool for the study of temperature increases due to ultrasound use.

390 Some final comments can be advanced about the material used for the test. Porcine
391 muscle was chosen because it has well-characterized acoustic and thermal properties, similar
392 to those reported for clinically relevant human soft tissues (Liang et al. 1991). There are
393 problems in relating laboratory animal studies to humans. We cannot extrapolate to humans
394 the results of studies performed on animals, or even from one animal species to another,
395 because differences in the results and conclusions may be due to strain differences.

396

397 CONCLUSION

398

399 SWE is a recent **diagnostic** ultrasound modality offering the possibility of a quantitative
400 assessment of tissue elasticity. It may have numerous potential applications in obstetric and
401 fetal imaging. The present study demonstrated the benefit of using surface temperature maps
402 captured by an IR camera for the analysis of heterogeneous heating caused by ultrasound. The
403 temperature rise in SWE mode appeared to be much higher compared to the other two modes
404 under study (B-mode and PD), as has already been indicated in thermocouple-based studies.
405 The IR thermography technique, in parallel with the thermocouple approach, could
406 advantageously be employed to study the safety of SWE in obstetrics. Tests on samples
407 containing both soft tissues and bones are also a perspective of this study. Finally, future
408 works could also concern the coupling of IR thermography with thermocouples placed inside
409 a phantom imitating biological tissue, in order to potentially reconstruct the variations in the
410 entire three-dimensional temperature field accompanying ultrasound.

411

412 ACKNOWLEDGEMENTS

413

414 The authors would like to thank Dr. Piero Miloro from National Physical Laboratory (NPL),
415 UK for the fruitful discussions about temperature rises due to elastography in tissues.

416

417

REFERENCES

418

419 Abramowicz JS. Ultrasound in obstetrics and gynecology: Is this hot technology too hot? J
420 Ultrasound Med 2012;21(12):1327–33.

421 Abramowicz JS, Barnett SB, Duck FA, Edmonds PD, Hynynen KH, Ziskin MC. Fetal
422 thermal effects of diagnostic ultrasound . J Ultrasound Med 2008;27(4):541–59.

423 Alan B, Goya C, Tunç S, Teke M, Hattapoğlu S. Assessment of placental stiffness using
424 acoustic radiation force impulse elastography in pregnant women with fetal anomalies.
425 Korean J Radiol 2016;17(2):218–23.

426 Ami O, Lamazou F, Mabilie M, Levailant JM, Deffieux X, Frydman R, Musset D. Real-time
427 transvaginal elastosonography of uterine fibroids. Ultrasound Obstet Gynecol
428 2009;34(4):486–88.

429 Barr RG, Nakashima K, Amy D, Cosgrove D, Farrokh A, Schafer F, Bamber JC, Castera L,
430 Choi BI, Chou YH, Dietrich CF, Ding H, Ferraioli G, Filice C, Friedrich-Rust M, Hall
431 TJ, Nightingale KR, Palmeri ML, Shiina T, Suzuki S, Sporea I, Wilson S, Kudo M.
432 WFUMB guidelines and recommendations for clinical use of ultrasound elastography:
433 Part 2: breast. Ultrasound Med Biol 2015;41(5):1148–60.

434 Bouchard RR, Dahl JJ, Hsu SJ, Palmeri ML, Trahey GE. Image quality, tissue heating, and
435 frame rate trade-offs in acoustic radiation force impulse imaging. IEEE Trans Ultrason
436 Ferroelectr Freq Control. 2009;56(1):63–76.

437 Chrysochoos A, Huon V, Jourdan F, Muracciole JM, Peyroux R, Wattrisse B. Use of full-
438 field digital image correlation and infrared thermography measurements for the
439 thermomechanical analysis of material behaviour. *Strain* 2010;46(1):117–130

440 Chrysochoos A and Surrel Y. Basics of metrology and introduction to techniques. In: Grediac
441 M and Hild F (Eds) *Full-field measurements and identification in solid mechanics*,
442 Wiley-ISTE, 2012. pp. 1–29

443 Church CC and Miller WM. Quantification of risk from fetal exposure to diagnostic
444 ultrasound. *Prog Biophys Mol Biol* 2007;93(1):331–53.

445 Cosgrove DO, Berg WA, Doré CJ, Skyba DM, Henry JP, Gay J, Cohen-Bacrie C. Shear wave
446 elastography for breast masses is highly reproducible. *Eur Radiol* 2012;22(5):1023–32.

447 Diguisto C, Simon EG, Callé S, Ternifi R, Remeniéras JP, Hervé P, Perrotin F. Ultrasonic
448 elastography exploration of the foetal brain: a case of atypical choroid plexus papilloma. *J*
449 *Obstet Gynaecol* 2017;37(4):525–27.

450 Ferraioli G, Filice C, Castera L, Choi BI, Sporea I, Wilson SR, Cosgrove D, Dietrich CF,
451 Amy D, Bamber JC, Barr R, Chou YH, Ding H, Farrokh A, Friedrich-Rust M, Hall TJ,
452 Nakashima K, Nightingale KR, Palmeri ML, Schafer F, Shiina T, Suzuki S, Kudo M.
453 WFUMB guidelines and recommendations for clinical use of ultrasound elastography:
454 Part 3: liver. *Ultrasound Med Biol* 2015;41(5):1161–79.

455 Fowlkes JB. American institute of ultrasound in medicine consensus report on potential
456 bioeffects of diagnostic ultrasound. *J Ultrasound Med* 2008;27(4):503–15.

457 Fruscalzo A, Mazza E, Feltovich H, Schmitz R. Cervical elastography during pregnancy: a
458 critical review of current approaches with a focus on controversies and limitations. *J Med*
459 *Ultrason* 2016;43(4):493–504.

460 Gennisson JL, Deffieux T, Fink M, Tanter M. Ultrasound elastography: Principles and
461 techniques. *Diagn Interv Imaging* 2013;94(5):487–95.

462 Germain MA, Webster WS, Edwards MJ. Hyperthermia as a teratogen: parameters
463 determining hyperthermia-induced head defects in the rat. *Teratology* 1985;31(2):265–
464 72.

465 Giering K, Minet O, Lamprecht I, Müller G. Review of thermal properties of biological
466 tissues. *SPIE PM* 1995;25:45–65

467 Gonzales RC and Woods RE. *Digital Image Processing*, third ed. Upper Saddle River, NJ:
468 Prentice-Hall, 2006

469 Grédiac M, Blaysat B, Sur F. A critical comparison of some metrological parameters
470 characterizing local Digital Image Correlation and Grid Method. *Exp Mech*
471 2017;57(6)871–903

472 Guibal A, Renosi G, Rode A, Scoazec JY, Guillaud O, Chardon L, Munteanu M, Dumortier J,
473 Collin F, Lefort T. Shear wave elastography: An accurate technique to stage liver fibrosis
474 in chronic liver diseases. *Diagn Interv Imaging* 2016;97(1):91–99.

475 Hernandez-Andrade E, Auriolles-Garibay A, Garcia M, Korzeniewski SJ, Schwartz AG, Ahn
476 H, Matinez-Varea A, Yeo L, Chaiworapongsa T, Hassan SS, Romero R. Effect of depth
477 on shear-wave elastography estimated in the internal and external cervical os during
478 pregnancy. *J Perinat Med* 2013;42(5):549–57.

479 Hinoue A, Fushiki S, Nishimura Y, Shiota K. In utero exposure to brief hyperthermia
480 interferes with the production and migration of neocortical neurons and induces apoptotic
481 neuronal death in the fetal mouse brain. *Brain Res Dev Brain Res* 2001;132(1):59–67.

482 Issaoui M, Debost-Legrand A, Skerl K, Chauveau B, Magnin B, Delabaere A, Boyer L,
483 Sauvart-Rochat MP, Lémery D. Shear wave elastography safety in fetus: a quantitative
484 health risk assessment. *Diagn Interv Imaging* 2018;99(9):519–24.

485 Khalil MR, Thorsen P, Uldbjerg N. Cervical ultrasound elastography may hold potential to
486 predict risk of preterm birth. *Dan Med J* 2013;60(1):A4570.

487 Kiliç F, Kayadibi Y, Yuksel MA, Adaletli I, Ustabaşıoğlu FE, Oncul M, Madazli R, Yılmaz
488 MH, Mihmanli I, Kantarci F. Shear wave elastography of placenta: in vivo quantitation of
489 placental elasticity in preeclampsia. *Diagn Interv Radiol* 2015;21(3):202–7.

490 Liang XG, Ge XS, Zhang YP, Wang GJ. A convenient method of measuring the thermal
491 conductivity of biological tissue. *Phys Med Biol* 1991;36(12):1599–1605.

492 Marinac-Dabic D, Krulewitch CJ, Moore RM Jr. The safety of prenatal ultrasound exposure
493 in human studies. *Epidemiology* 2002;13 Suppl 3:S19–22.

494 Miloro P, Eleanor M, Adam S. Temperature elevation measured in a tissue-mimicking
495 phantom for transvaginal ultrasound at clinical settings. *Ultrasound* 2017;25(1):6–15.

496 Molina FS, Gómez LF, Florido J, Padilla MC, Nicolaidis KH. Quantification of cervical
497 elastography: a reproducibility study. *Ultrasound Obstet Gynecol* 2012;39(6):685–89.

498 Mottet N, Aubry S, Vidal C, Boiteux G, Metz JP, Riethmuller D, Pazart L, Ramanah R.
499 Feasibility of 2-D ultrasound shear wave elastography of fetal lungs in case of threatened
500 preterm labour: a study protocol. *BMJ Open* 2017;7(12):e018130.

501 Nitta N, Ishiguro Y, Sasanuma H, Taniguchi N, Akiyama I. Experimental system for in-situ
502 measurement of temperature rise in animal tissue under exposure to acoustic radiation
503 force impulse. *J Med Ultrason (2001)* 2015;42(1):39–46.

504 O'Hara S, Zelesco M, Sun Z. Shear wave elastography on the uterine cervix: technical
505 development for the transvaginal approach. *J Ultrasound Med* 2018;
506 <https://doi.org/10.1002/jum.14793>

507 Palmeri ML and Nightingale KR. On the thermal effects associated with radiation force
508 imaging of soft tissue. *IEEE Trans Ultrason Ferroelectr Freq Control* 2004;51(5):551–65.

509 Pellicer B, Herraiz S, Táboas E, Felipe V, Simon C, Pellicer A. Ultrasound bioeffects in rats:
510 quantification of cellular damage in the fetal liver after pulsed doppler imaging.
511 *Ultrasound Obstet Gynecol* 2011;37(6):643–48.

512 Quarello E, Lacoste R, Mancini J, Melot–Dusseau S, Gorincour G. Shear wave elastography
513 of fetal lungs in pregnant baboons. *Diagn Interv Imaging* 2016;97(6):605–10.

514 Schneider-Kolsky ME, Ayobi Z, Lombardo P, Brown D, Kedang B, Gibbs ME. Ultrasound
515 exposure of the foetal chick brain: effects on learning and memory. *Int J Dev Neurosci*
516 2009;27(7):677–83.

517 Shankar H and Pagel PS. Potential adverse ultrasound-related biological effects: a critical
518 review. *Anesthesiology* 2011;115(5):1109–24.

519 Shiina T, Nightingale KR, Palmeri ML, Hall TJ, Bamber JC, Barr RG, Castera L, Choi BI,
520 Chou YH, Cosgrove D, Dietrich CF, Ding H, Amy D, Farrokh A, Ferraioli G, Filice C,
521 Friedrich-Rust M15, Nakashima K, Schafer F, Sporea I, Suzuki S, Wilson S, Kudo M.
522 WFUMB guidelines and recommendations for clinical use of ultrasound elastography:
523 Part 1: basic principles and terminology. *Ultrasound Med Biol* 2015;41(5):1126–47.

524 Skurczynski MJ, Duck FA, Shipley JA, Bamber JC, Melodelima D. Evaluation of
525 experimental methods for assessing safety for ultrasound radiation force elastography.
526 *Brit J Radiol* 2009;82(980):666–74.

527 Tabaru M, Yoshikawa H, Azuma T, Asami R, Hashiba K. Experimental study on temperature
528 rise of acoustic radiation force elastography. *J Med Ultrason (2001)* 2012;39(3):137–46.

529 Thomas A, Kümmel S, Gemeinhardt O, Fischer T. Real-time sonoelastography of the cervix:
530 tissue elasticity of the normal and abnormal cervix. *Acad Radiol* 2007;14(2):193–200.

531 Ziskin MC and Morrissey J. Thermal thresholds for teratogenicity, reproduction, and
532 development. *Int J Hyperthermia* 2011;27(4):374–87.

533

534 **Figure captions list**

535

536 **Fig. 1** Experimental setup: a) two tested configurations, b) schematic views of Configuration
537 #1, c) photographs of the experiment involving a curved transducer.

538 **Fig. 2.** Illustration of the benefit of using the reference sample. Data correspond here to a test
539 performed in Configuration #1 for B-mode.

540 **Fig. 3.** Maps of temperature change at $t = 80$ s for Configuration #1: a) B-mode, b) PD,
541 c) SWE. The color scale is the same as in Figs. 4-a and -b for comparison purposes.
542 d) Snapshots of the central zone with suitable color scales.

543 **Fig. 4.** Maps of temperature change at $t = 360$ s for Configuration #1: a) B-mode, b) PD,
544 c) SWE.

545 **Fig. 5.** Maps of temperature change at $t = 360$ s for Configuration #2: a) B-mode, b) PD,
546 c) SWE.

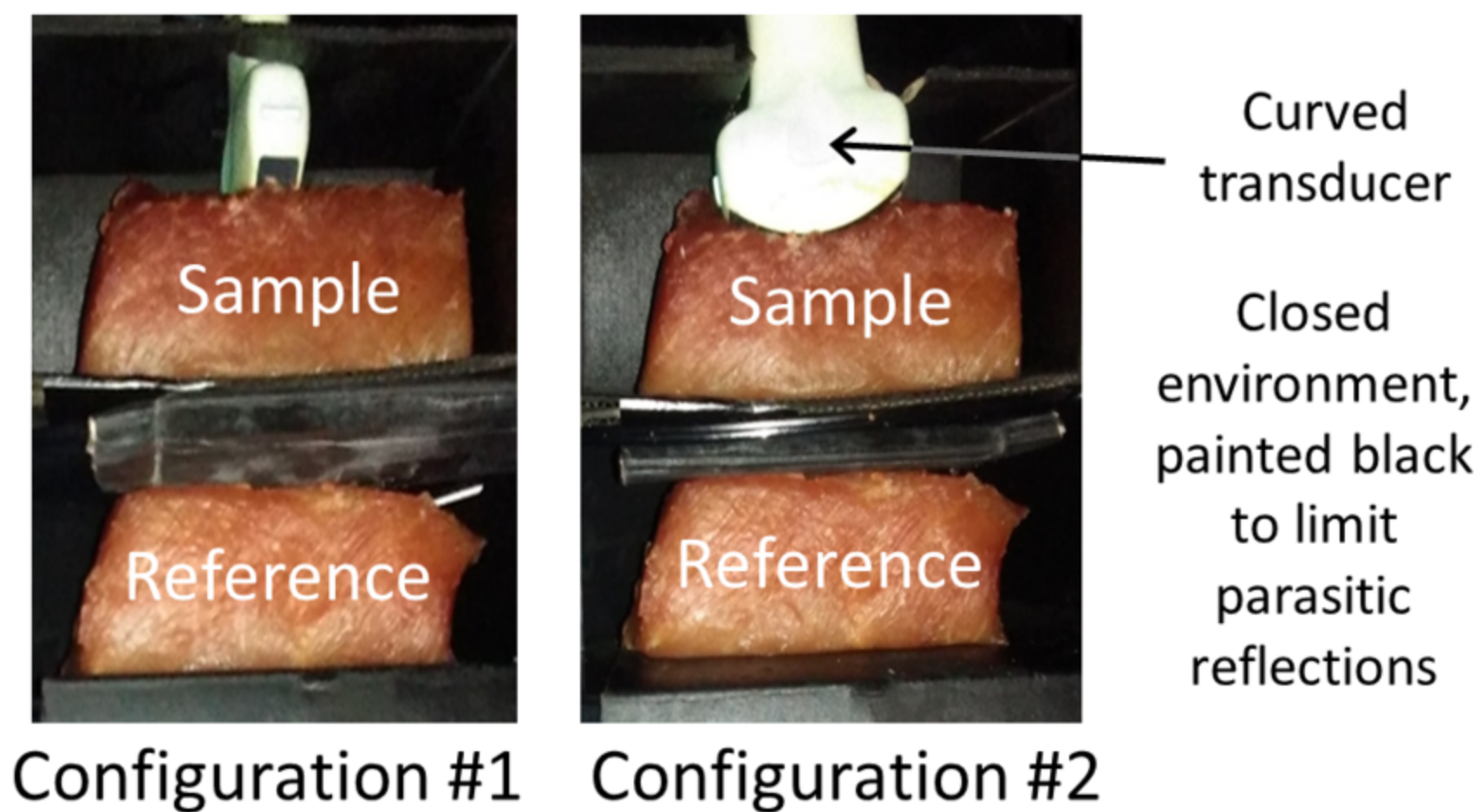
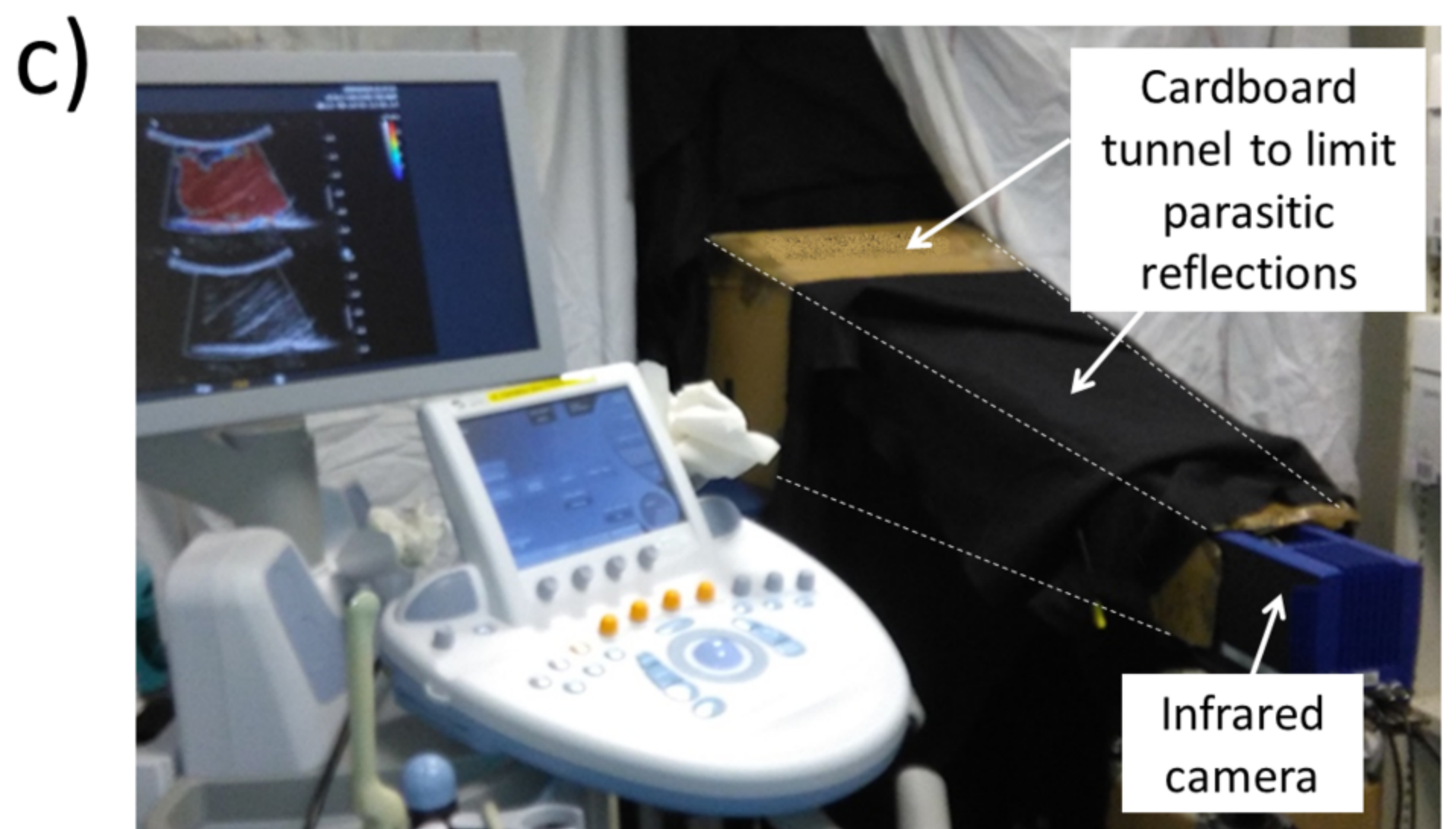
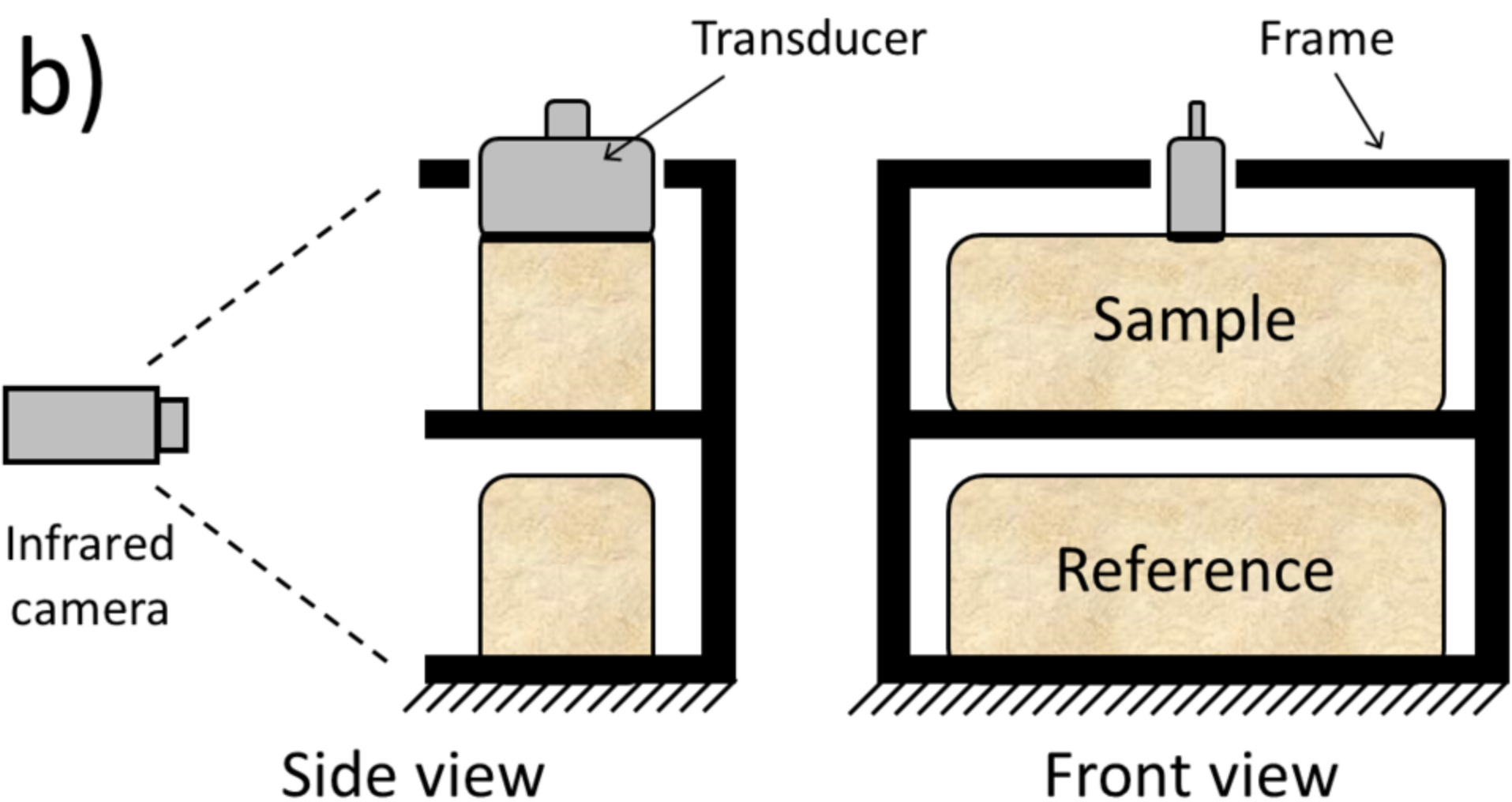
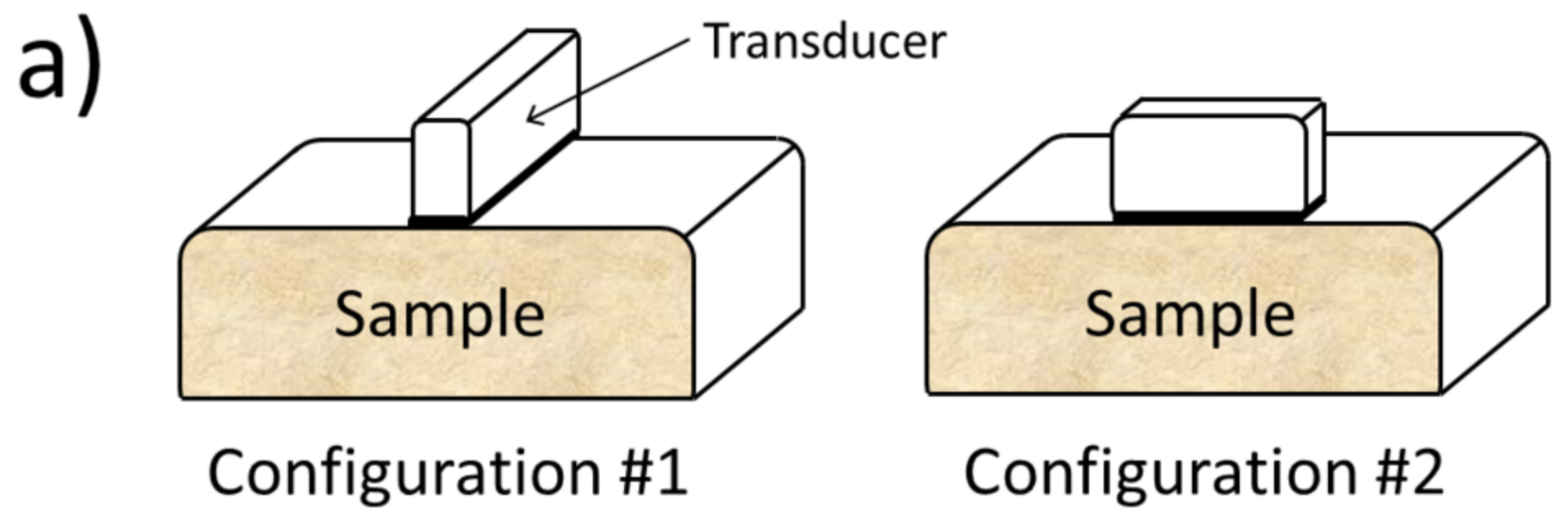
547 **Fig. 6.** Temperature change at points A and B for a) Configuration #1 and b) Configuration
548 #2, respectively. The vertical dashed lines correspond to the end of transducer activation.

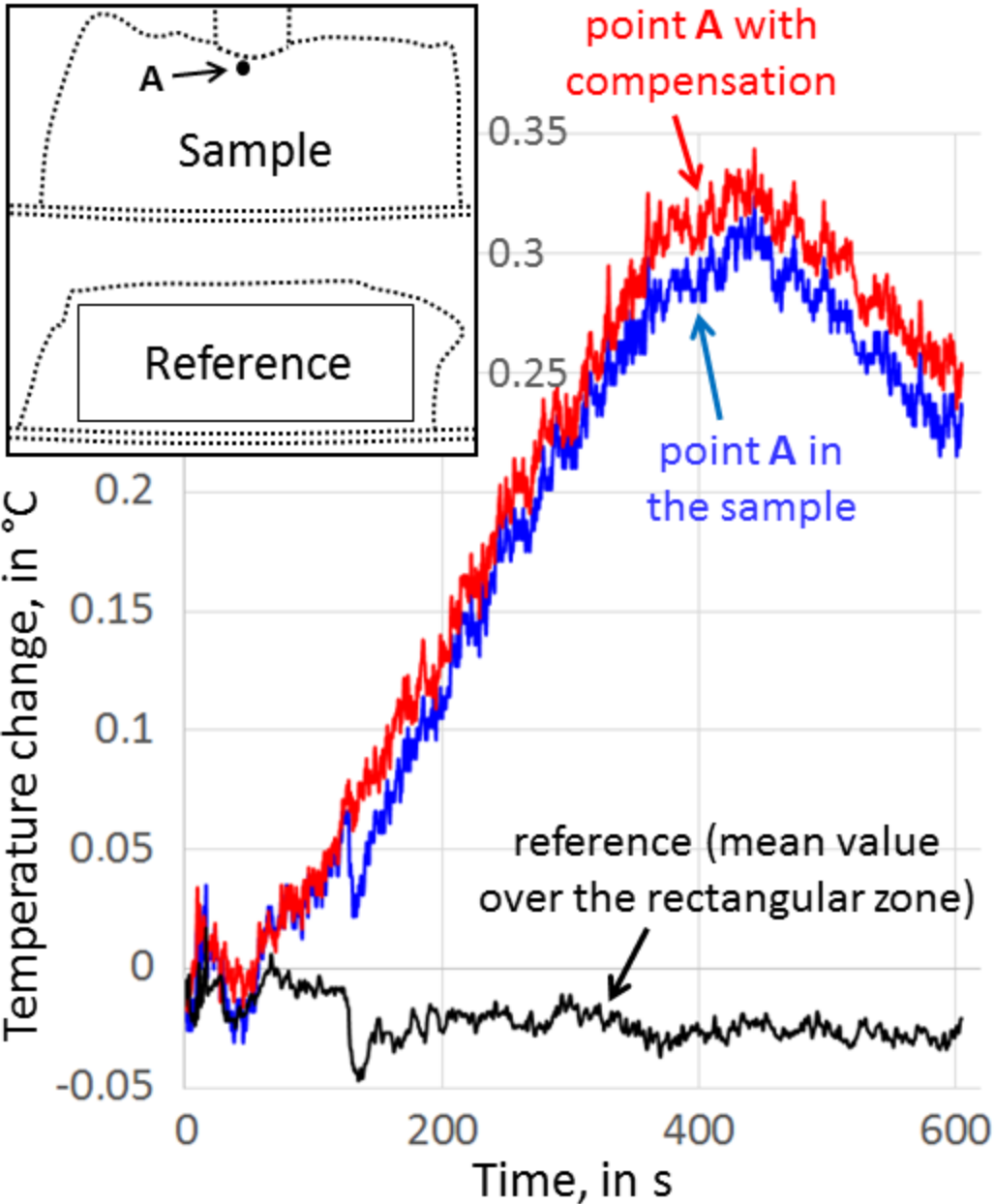
549 **Fig. 7.** Temperature change at point C for Configuration #2, for comparison purposes with
550 point A in Configuration #1 (compare with in Fig. 6-a). The vertical dashed line corresponds
551 to the end of transducer activation. The hatched area corresponds to the part of the sample
552 which is not present in Configuration #1.

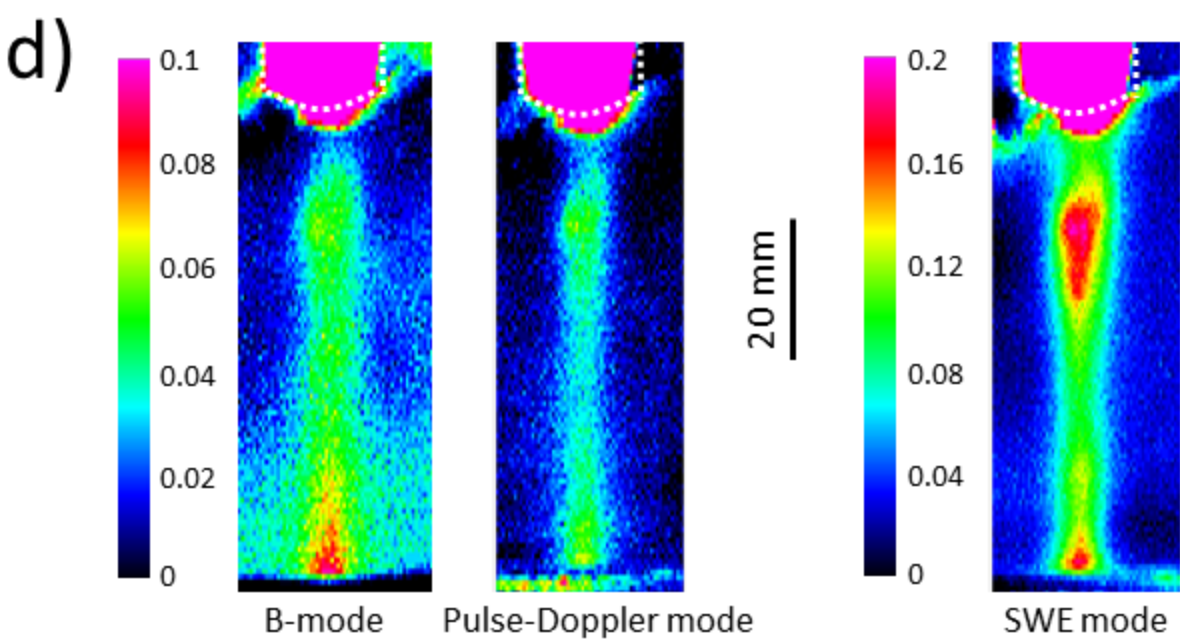
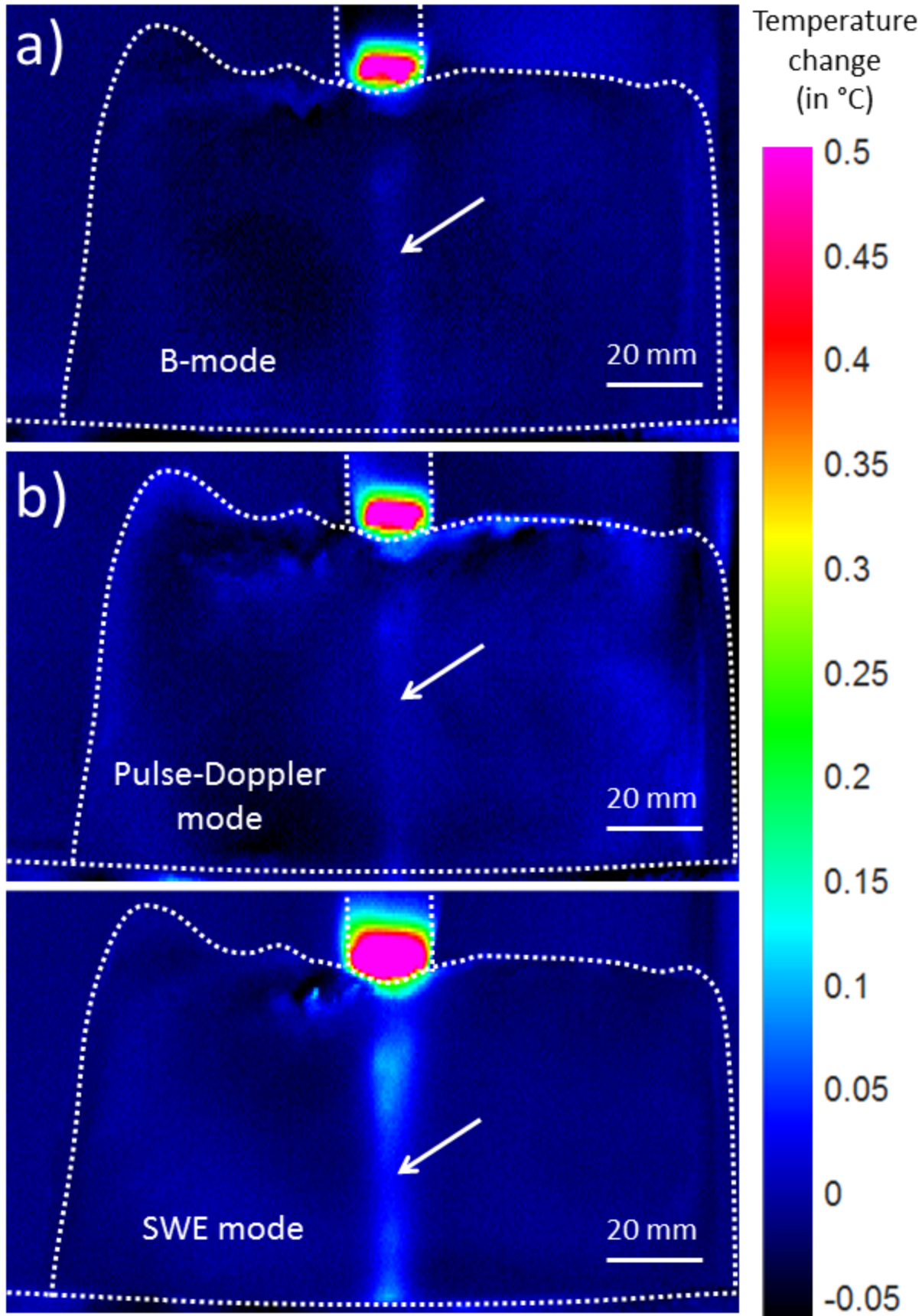
553 **Fig. 8.** B-mode: a) temperature change as a function of time in Configuration #1, b) same in
554 Configuration #2. The vertical dashed lines correspond to the end of transducer activation.

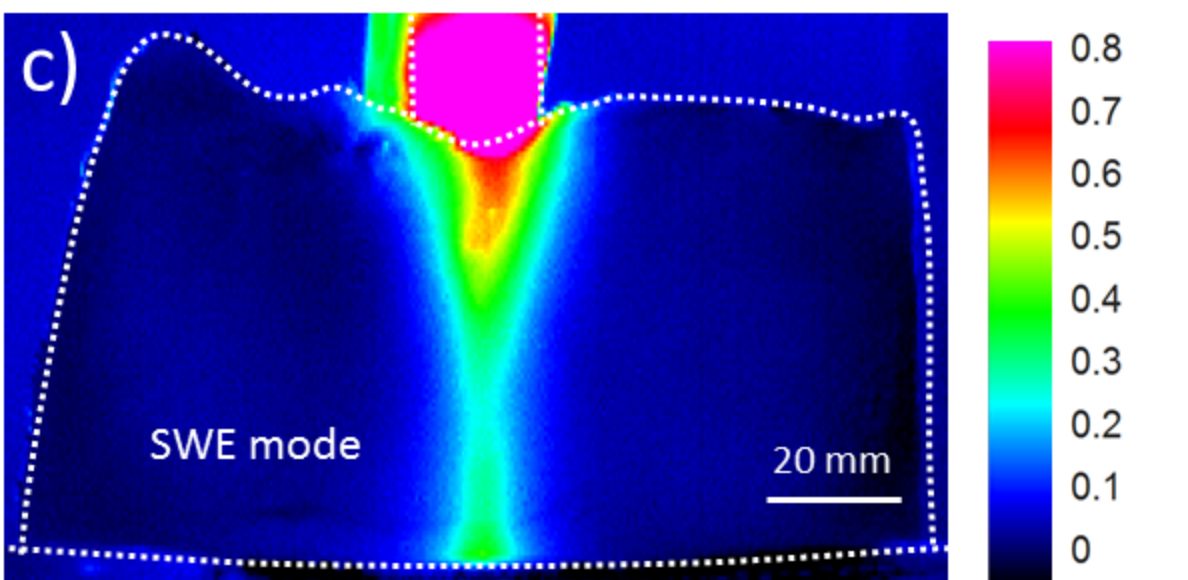
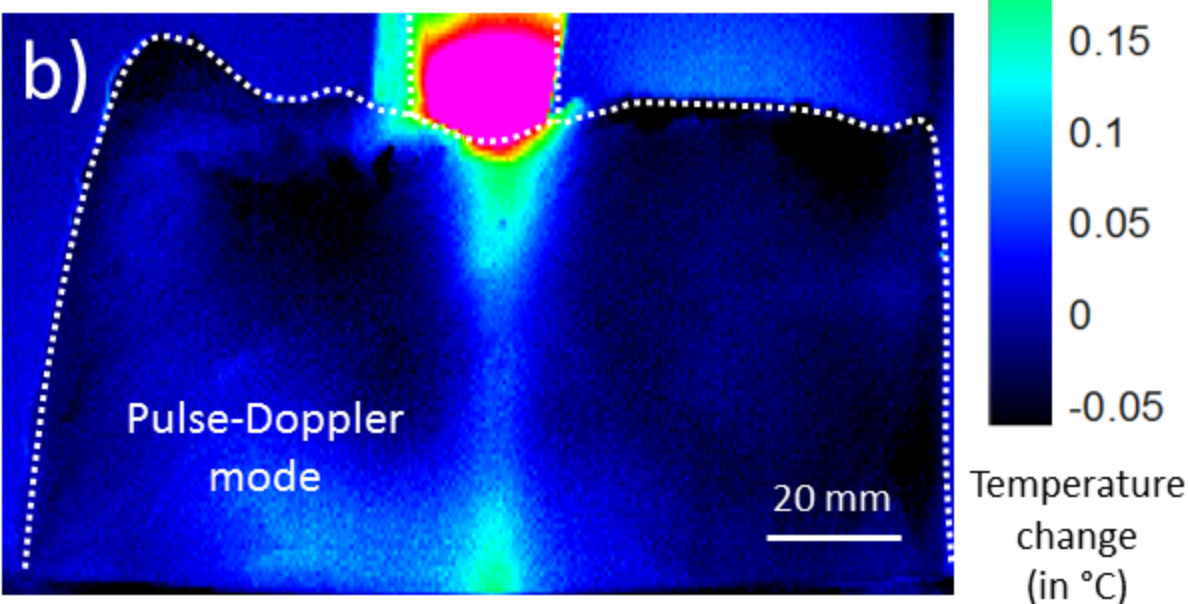
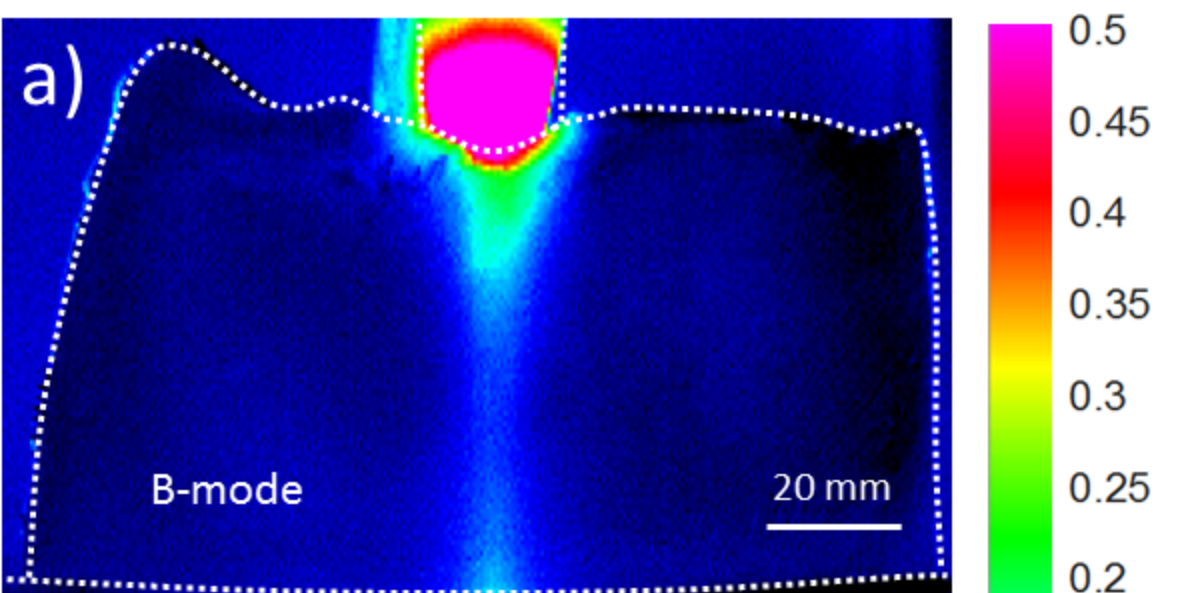
555 **Fig. 9** Temperature change as a function of time for the Pulse-Doppler mode: a) in
556 Configuration #1, b) in Configuration #2. Location of the points is the same as in Figs. 8-a
557 and -b. The vertical dashed lines correspond to the end of transducer activation

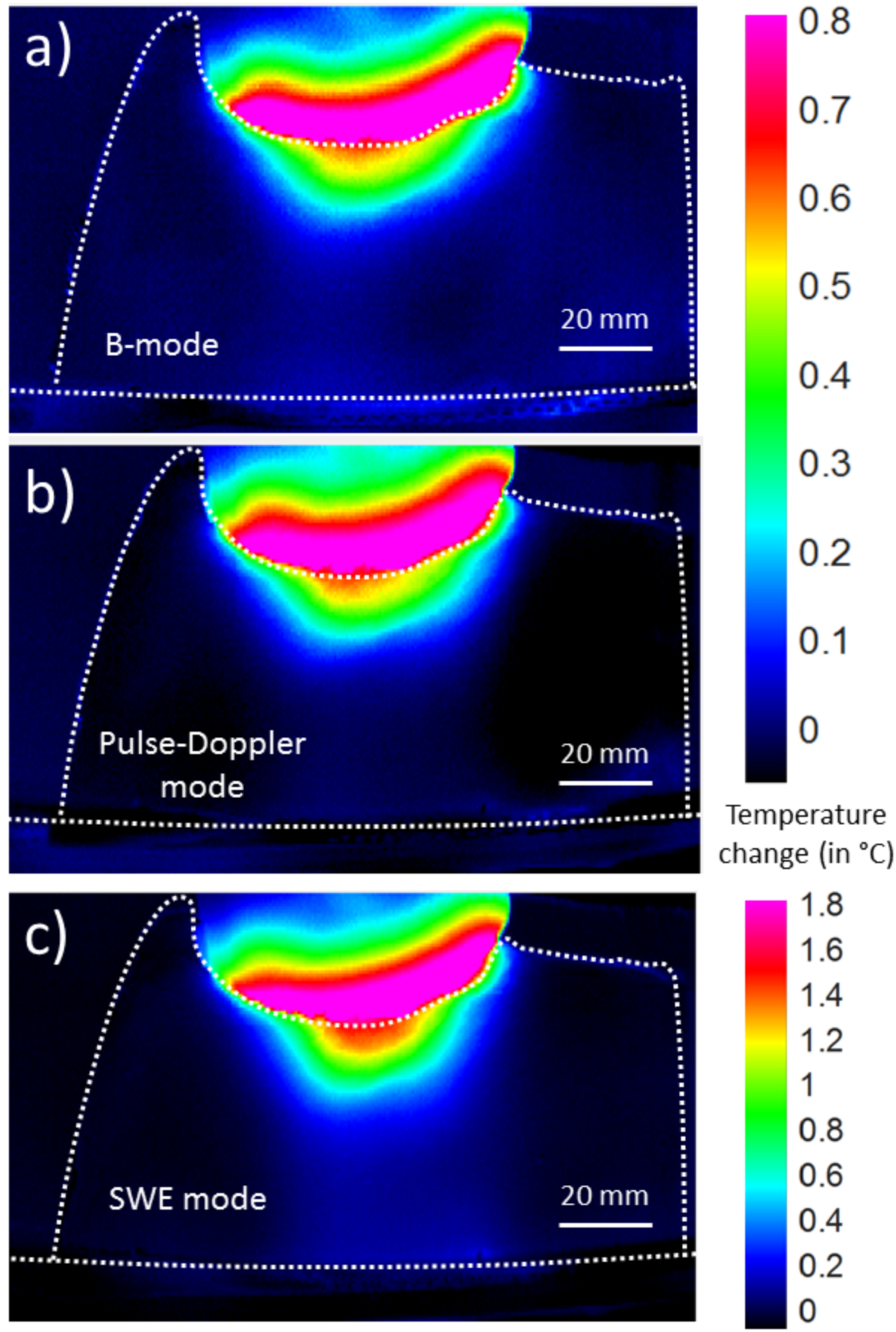
558 **Fig. 10** Temperature change as a function of time for the SWE mode: a) in Configuration #1,
559 b) in Configuration #2. Location of the points is the same as in Figs. 8-a and -b. The vertical
560 dashed lines correspond to the end of transducer activation

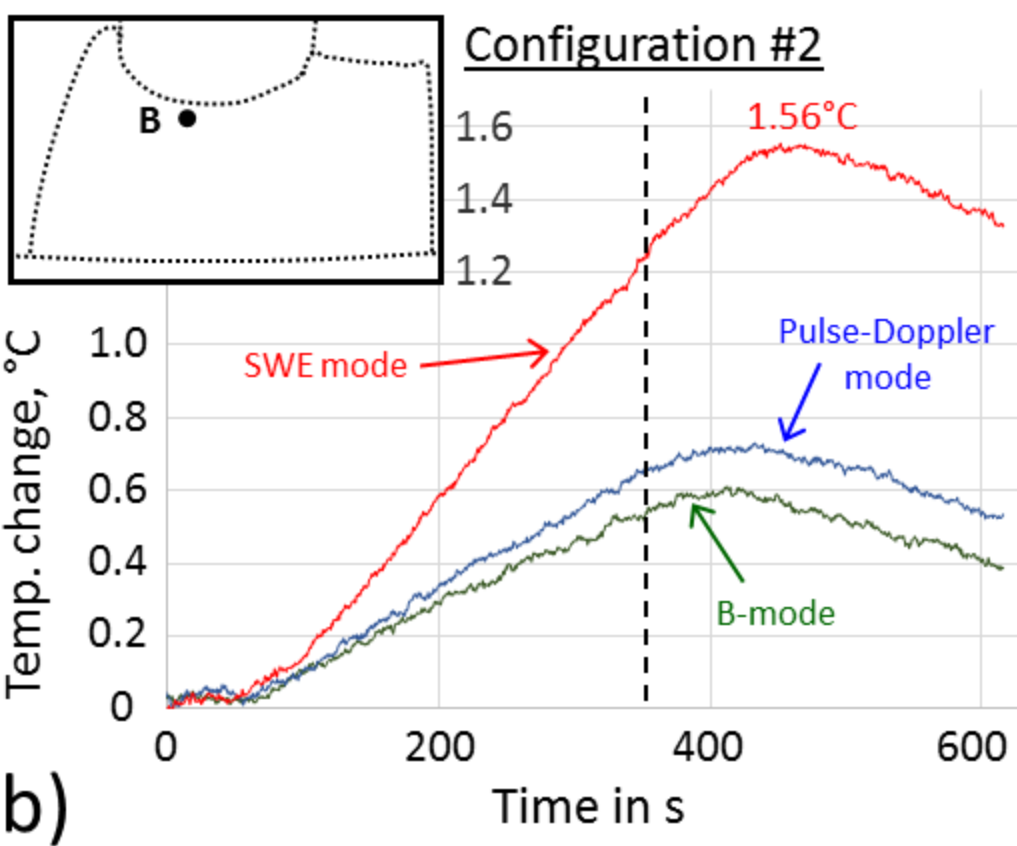
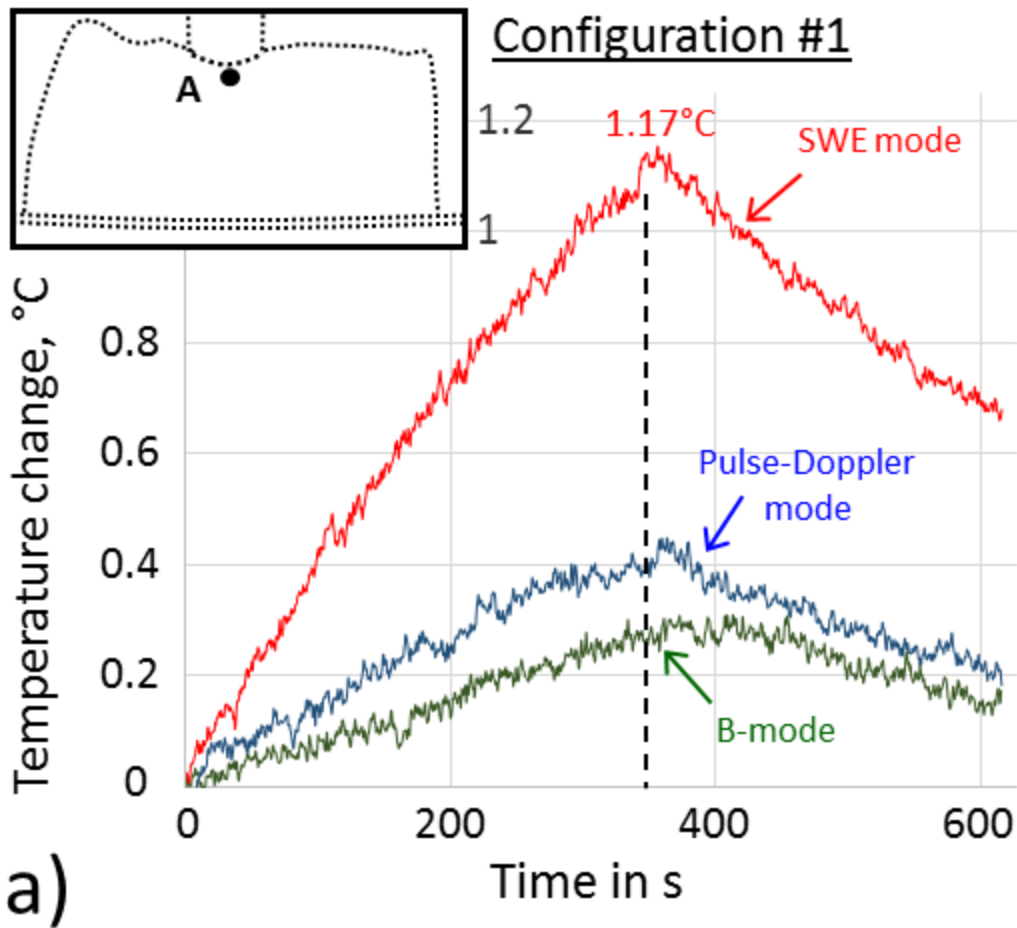






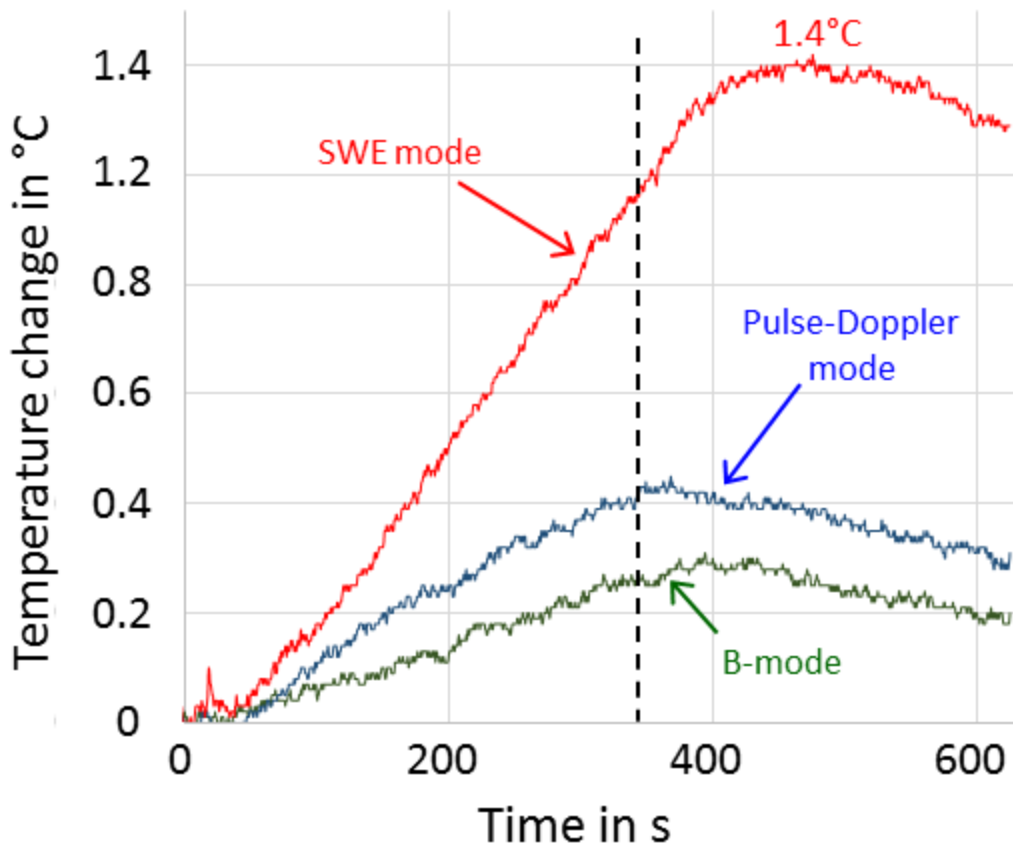
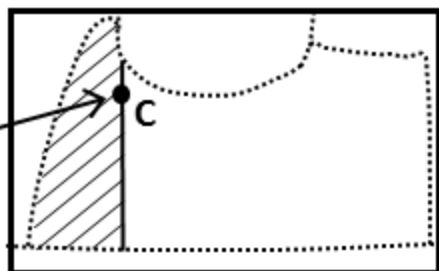


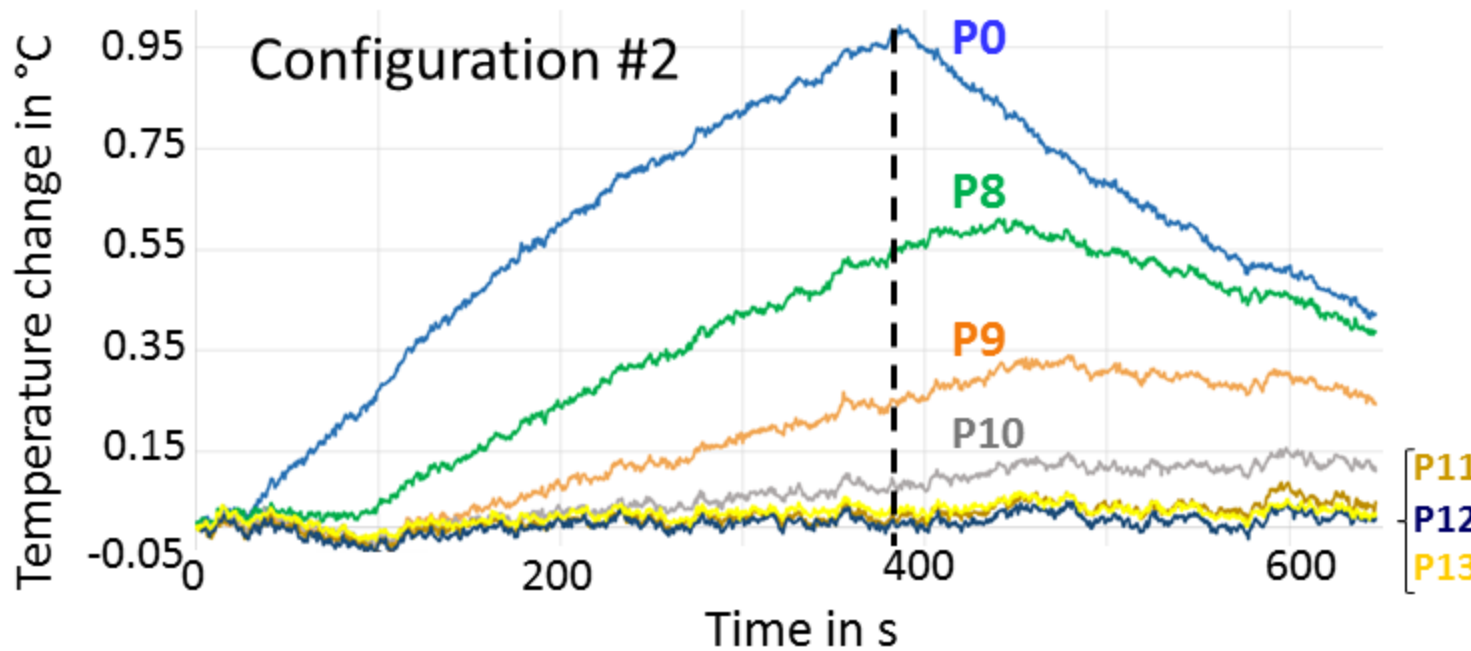
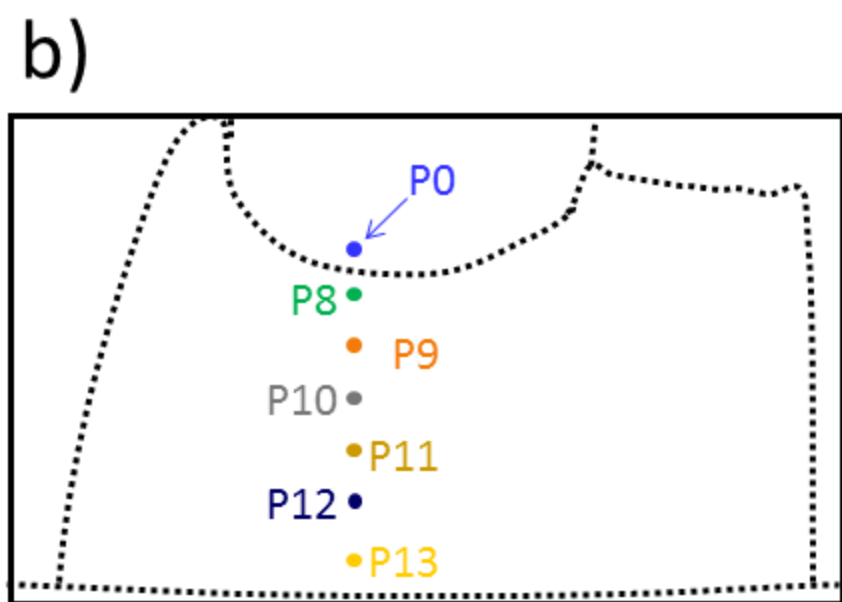
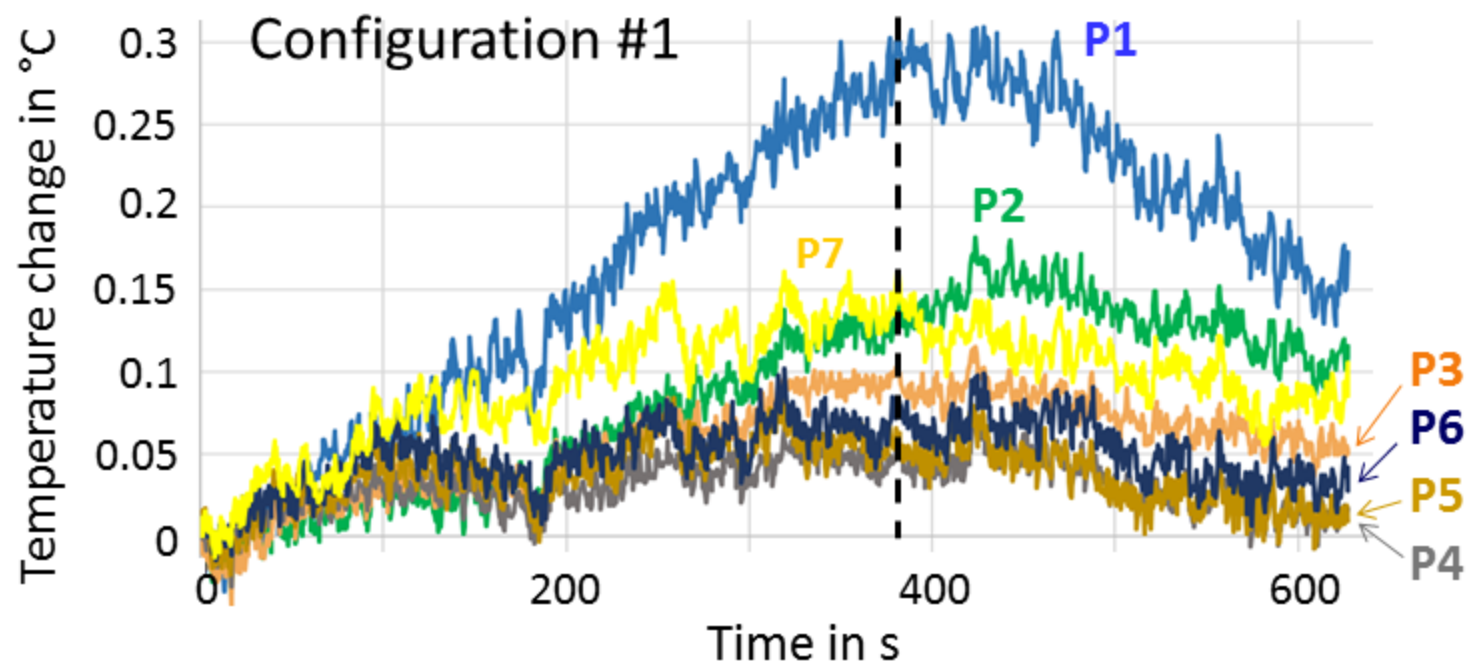
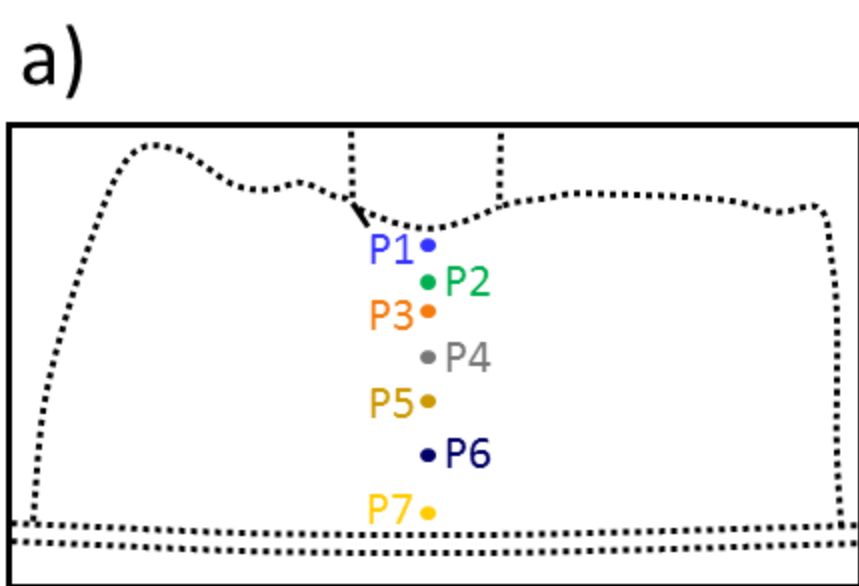


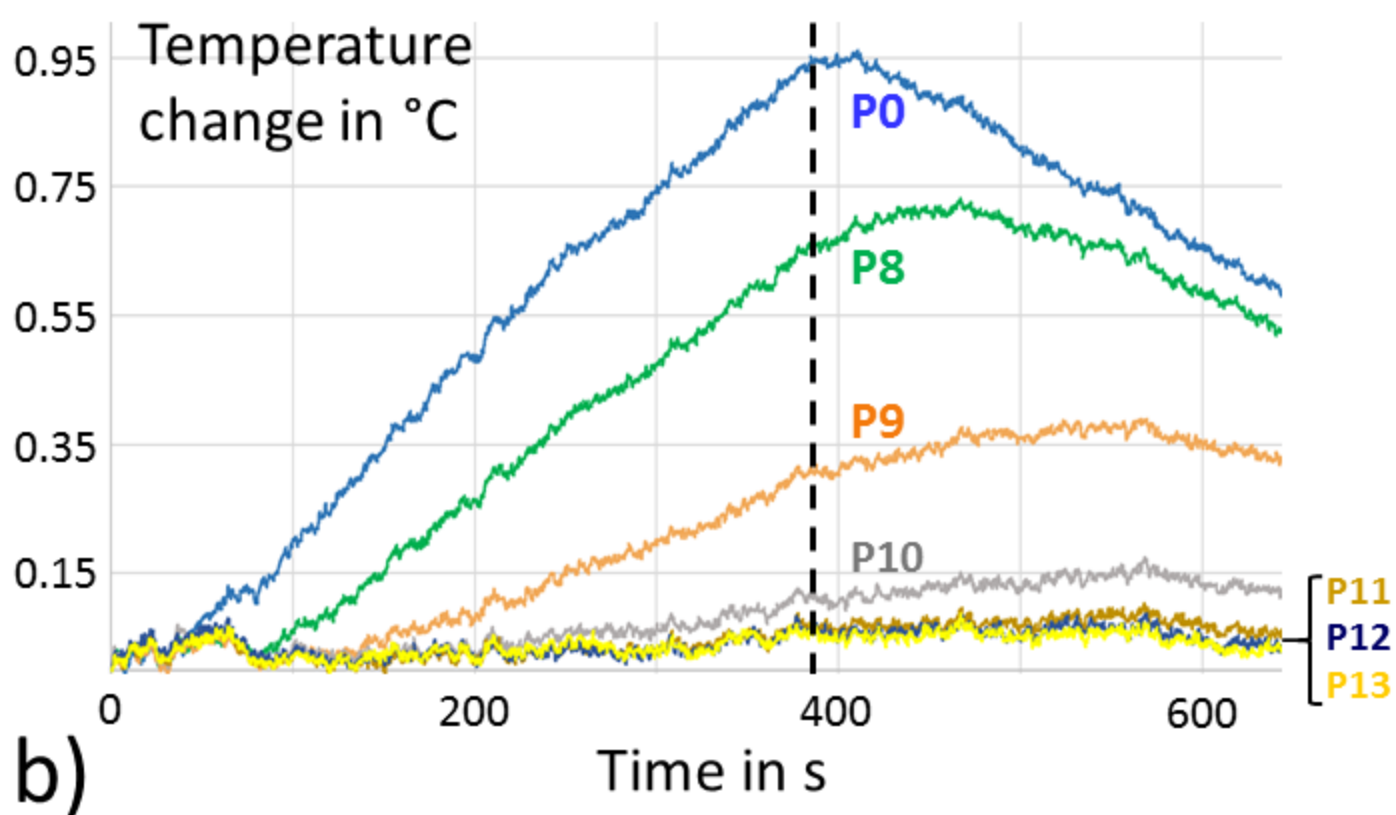
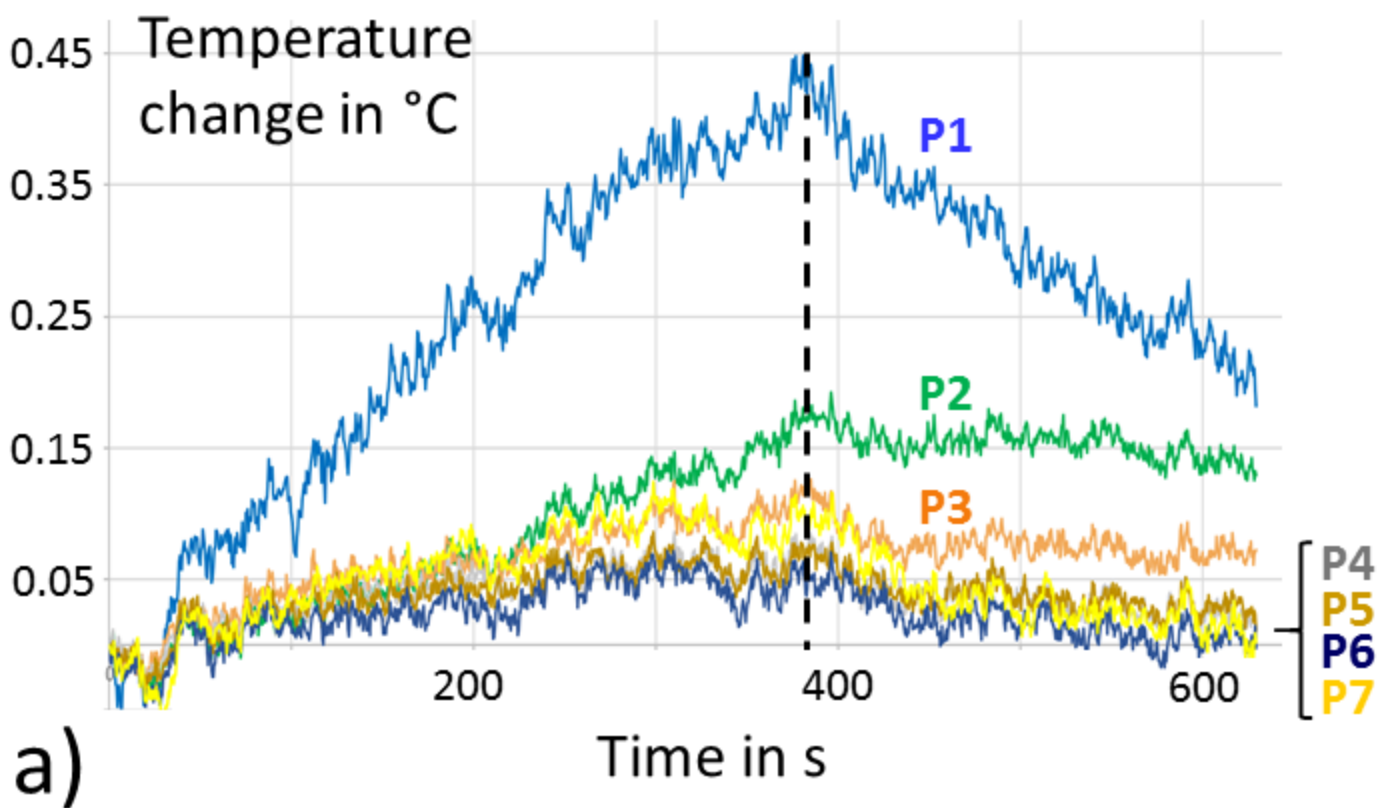


Configuration #2

≈ Point A in
configuration #1







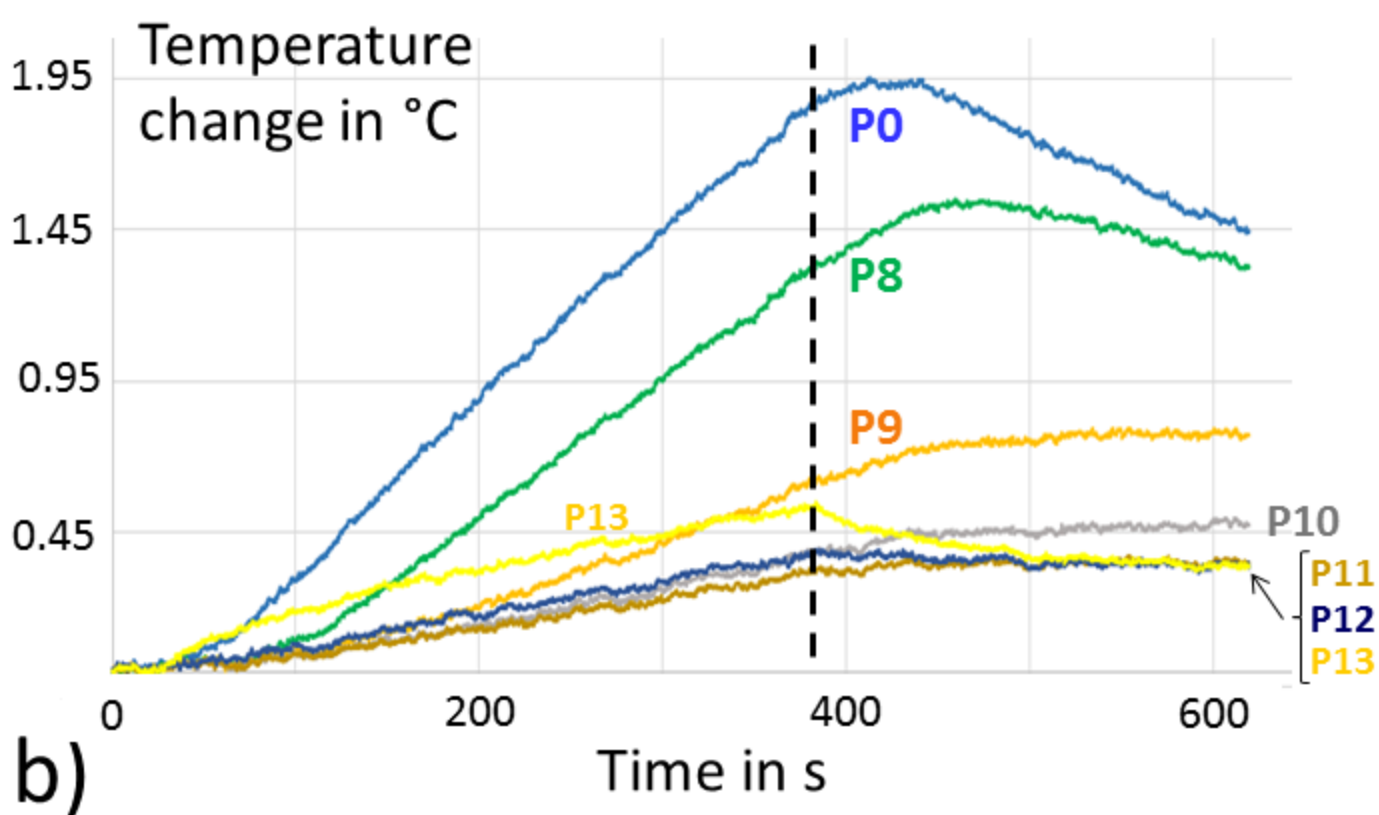
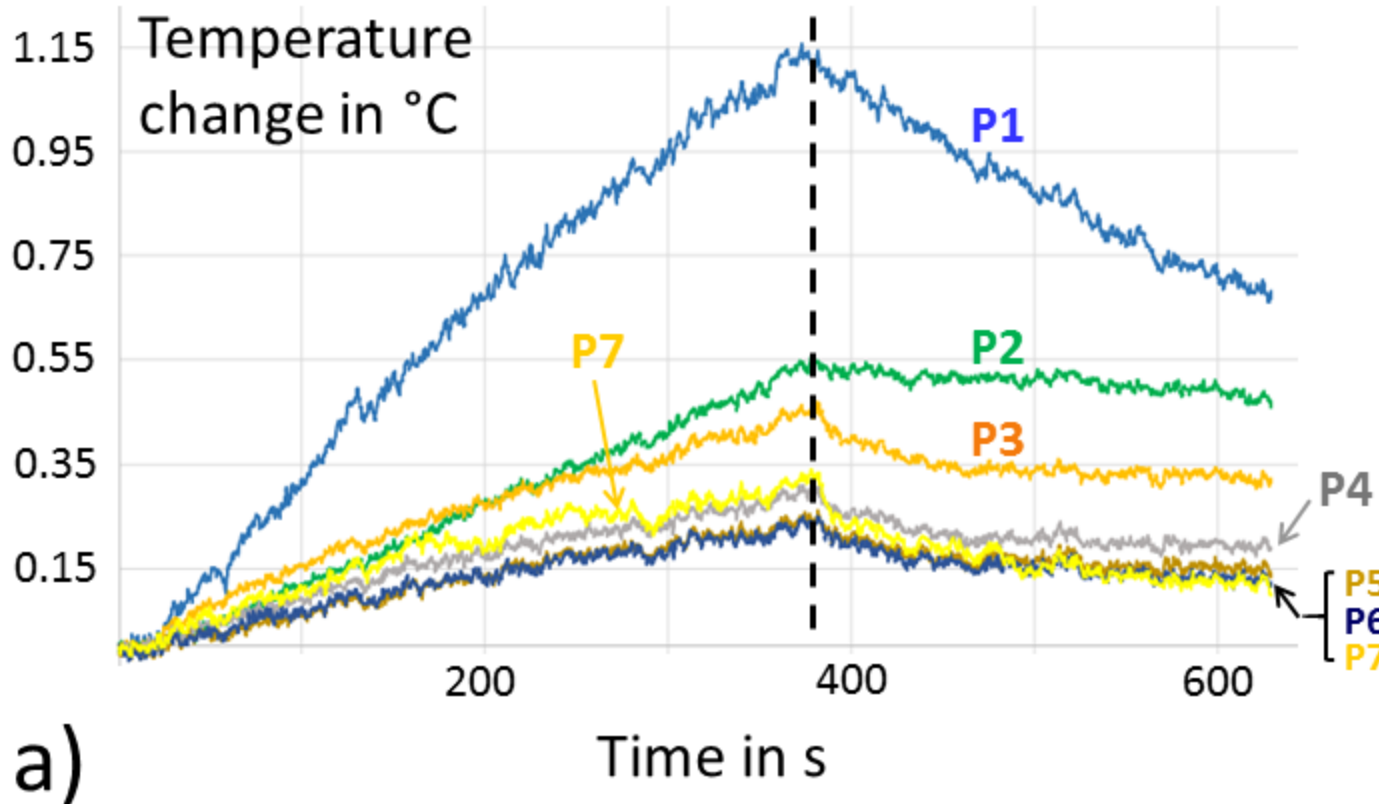


Table 1. Parameters for the three ultrasound modes used.

Parameters (OB-GYN GenOB preset)	B-mode	PD	SWE	Comment
Total depth	70 mm	22 mm	70 mm	
B-mode focal zone	10 – 25 mm	22 mm	25 – 40 mm	
Tissuetuner	1540 m/s	1540 m/s	1540 m/s	Speed of sound used to transmit and receive beamforming
SWE Opt (Res, Std, Pen)	N/A	N/A	Standard	Optimization of elastography resolution and penetration
SWE box geometry	N/A	N/A	Top width: 43.9 mm Bottom width: 63.2 mm Height: 30.8 mm Top depth: 6.7 mm	
MI	1.2	1	1.5	Mechanical Index
TIb	0	0	1.6	Thermal Index bone
TI _s	0	0	1.4	Thermal Index soft tissue
Ispta	< 720 mW/cm ²	< 720 mW/cm ²	< 720 mW/cm ²	Spatial-peak temporal-average intensity